1 **Main Manuscript for**

2 Unexpected anthropogenic emission decreases explain recent atmospheric

3 mercury concentration declines

4

5 Aryeh Feinberg[a]*, Noelle E. Selin[a,b], Christine F. Braban[c], Kai-Lan Chang[d,e], Danilo Custódio[f], Daniel A.

6 Jaffe[g,h], Katriina Kyllönen[i], Matthew S. Landis[j], Sarah R. Leeson[c], Winston Luke[k], Koketso M. Molepo[l],

7 Marijana Murovec[m], Michelle G. Nerentorp Mastromonaco[n], Katrine Aspmo Pfaffhuber[o], Julian Rüdiger[p],

8 Guey-Rong Sheu[q], and Vincent L. St.Louis[r]

9 [a] *Institute for Data, Systems, and Society, Massachusetts Institute of Technology, Cambridge, MA 02139,*

10 *USA*

11 [b] *Department of Earth, Atmospheric, and Planetary Sciences, Massachusetts Institute of Technology,*

12 *Cambridge, MA 02139, USA*

13 [c] *UK Centre for Ecology & Hydrology (UKCEH), Penicuik, Midlothian EH26 0QB, UK*

14 [d] *Cooperative Institute for Research in Environmental Sciences, University of Colorado, Boulder, CO*

15 *80309-0401, USA*

16 [e] *NOAA Chemical Sciences Laboratory, Boulder, CO 80305, USA*

17 [f] *Max-Planck-Institut für Biogeochemie, D-07745 Jena, Germany*

18 [g] *School of STEM, University of Washington Bothell, Bothell, WA 98011, USA*

19 [h] *Department of Atmospheric Sciences, University of Washington Seattle, Seattle, WA 98195, USA*

20 [i] *Finnish Meteorological Institute, Helsinki 00560, Finland*

21 [j] *United States Environmental Protection Agency, Office of Research and Development, Research*

22 *Triangle Park, NC 27711, USA*

23 [k] *NOAA/Air Resources Laboratory, College Park, MD 20740, USA*

24 [l] *Institute of Coastal Environmental Chemistry, Helmholtz Zentrum Hereon, 21502 Geesthacht, Germany*

25 [m] *Slovenian Environment Agency, Environment and Nature protection Office, Air Quality Division,1000*

26 *Ljubljana, Slovenia*

27 [n] *IVL Swedish Environmental Research Institute, SE-411 33 Gothenburg, Sweden*

28 [o] *NILU, 2027 Kjeller, Norway*

29 [p] *Air Monitoring Network, German Environment Agency, 63225 Langen, Germany*

30 [q] *Department of Atmospheric Sciences, National Central University, Taoyuan 320, Taiwan*

31 [r] *Department of Biological Sciences, University of Alberta, Edmonton, AB T6G 2E9, Canada*

32

33 *Correspondence to: arifeinberg@gmail.com (A.F.)

34

35

36 **Author Contributions:** A.F. and N.E.S. designed the research. K.-L.C. advised the implementation of
37 statistical methods. C.F.B., D.C., D.A.J., K.K., M.S.L., S.R.L., W.L., K.M.M., M.M., M.G.N.M., K.A.P., J.R.,
38 G.-R.S., and V.L.S.L. contributed Hg observation data. A.F. performed the analysis and wrote the
39 manuscript under the supervision of N.E.S., with inputs and discussion from all authors. Author order is
40 alphabetical following the second author, N.E.S.

41

43

44 **Classification:** Physical Sciences/Earth, Atmospheric, and Planetary Sciences

45

48

49 **This PDF file includes:**
50      Main Text
51      Figures 1 to 4
52      Table 1
53

54 **Abstract**
55 Anthropogenic activities emit ~2000 Mg yr$^{-1}$ of the toxic pollutant mercury (Hg) into the atmosphere,
56 leading to long-range transport and deposition to remote ecosystems. Global anthropogenic emissions
57 inventories report increases in Northern Hemispheric (NH) Hg emissions during the last three decades, in
58 contradiction with the observed decline in atmospheric Hg concentrations at NH measurement stations.
59 Many factors can obscure the link between anthropogenic emissions and atmospheric Hg concentrations,
60 including trends in the re-emissions of previously released anthropogenic ("legacy") Hg, atmospheric sink
61 variability, and spatial heterogeneity of monitoring data. Here we assess the observed trends in gaseous
62 elemental mercury (Hg$^0$) in the NH and apply biogeochemical box modeling and chemical transport
63 modeling to understand the trend drivers. Using linear mixed effects modeling of observational data from
64 51 stations, we find negative Hg$^0$ trends in most NH regions, with an overall trend for 2005–2020 of
65 -0.011 ± 0.006 ng m$^{-3}$ yr$^{-1}$ (±2 SD). In contrast to existing emission inventories, our modelling analysis
66 suggests that NH anthropogenic emissions must have declined by at least 140 Mg yr$^{-1}$ between the years
67 2005 and 2020 to be consistent with observed trends. Faster declines in 95$^{th}$ percentile Hg$^0$ values than
68 median values in Europe, North America, and East Asian measurement stations corroborate that the
69 likely cause is a decline in nearby anthropogenic emissions rather than background legacy re-emissions.
70 Our results are relevant for evaluating the effectiveness of the Minamata Convention on Mercury,
71 demonstrating that existing emissions inventories are incompatible with the observed Hg$^0$ declines.
72

73 **Significance statement**
74 Mercury (Hg) is a global pollutant that bioaccumulates to toxic concentrations along the food chain.
75 Anthropogenic Hg inventories suggest increasing global emissions over recent decades, which is at odds
76 with observed declines of atmospheric Hg concentrations in the Northern Hemisphere (NH). We use
77 statistical and process-based modeling to rule out the possibility that NH anthropogenic emissions of Hg
78 could have increased while atmospheric Hg concentrations declined. This implies that anthropogenic
79 emissions of Hg have very likely declined in recent years. This work informs the effectiveness evaluation
80 of the international Minamata Convention on Mercury. Further research is required to better link emission
81 changes with measured concentrations so that the specific causes of global Hg trends can be identified.
82
83 **Main Text**
84
85 **Introduction**
86 The global Minamata Convention on Mercury is a multilateral environmental agreement that aims to
87 "protect human health and the environment from anthropogenic emissions and releases of mercury", a
88 neurotoxic pollutant (1). As mercury (Hg) is volatile and long-lived (~6 months) in the atmosphere (2),
89 trends in atmospheric mercury concentrations are one of the proposed indicators that will be used to
90 evaluate the Convention's effectiveness (3). However, linking trends in Hg concentrations and
91 anthropogenic emissions is not a straightforward process. The major anthropogenic emissions sources of
92 Hg, including artisanal and small-scale gold mining (ASGM), coal combustion, and industrial processes,
93 are distributed heterogeneously across the globe (4, 5). At the same time, legacy re-emissions of
94 historical anthropogenic mercury from soils, freshwater, wildfires, and oceans are diffuse background
95 sources, which are thought to make up a larger fraction of the overall Hg source fluxes (60% for legacy
96 re-emissions vs. 27% for primary anthropogenic) (6). Atmospheric Hg monitoring stations are also not
97 evenly distributed globally, with more stations located in North America and Europe (7), and they cover
98 different time periods. Therefore, statistical modeling is necessary to maximize the information present in
99 atmospheric Hg records (8), while mechanistic modeling helps connect observed Hg concentrations with
100 their drivers, i.e., emissions, chemical transformations, transport, and deposition (7).
101

102  The large-scale trends of atmospheric Hg over the last three decades have been under recent debate.
103  Bottom-up inventories show increasing global anthropogenic emissions since the 1990s (5, 9, 10), which,
104  all else being equal, should increase atmospheric Hg concentrations. However, in North America and
105  Europe, measured gaseous elemental mercury (GEM: $Hg^0$) concentrations have generally been declining
106  since continuous measurements began in the 1990s (7, 11–14). There is a clear need to understand this
107  contradiction and evaluate past trends of Hg emissions, especially after the adoption of the Minamata
108  Convention in 2013. Zhang et al. (7), the most recent study to evaluate the consistency between emission
109  inventories and atmospheric observations using the chemical-transport model GEOS-Chem, analyzed
110  available data through 2014. Their comparison between the model and measurements from North
111  America and Europe led the authors to conclude that anthropogenic Hg emissions declined by ~30%
112  between 1990 and 2010, due to weaker increases of Hg emissions from ASGM and strong declines in Hg
113  emissions from commercial products (7). More recent measurements from East Asian stations have also
114  reported declines in atmospheric Hg (15–18). Long term measurements from the Southern Hemisphere
115  (SH) remain scarce, with the latest results from the observation stations Cape Point and Amsterdam
116  Island showing insignificant trends between 2012–2017 (19). Alternative hypotheses have been proposed
117  to explain the decline in atmospheric Hg in the Northern Hemisphere (NH) while anthropogenic emissions
118  rise, including increased elemental mercury ($Hg^0$) uptake by vegetation (20) and declining Hg emissions
119  from ocean legacy re-emissions due to reduced anthropogenic inputs after the 1970s (21, 22). However,
120  a decline in legacy emissions of Hg is difficult to reconcile with biogeochemical box models, which
121  suggest that legacy Hg emissions generally increase if anthropogenic emissions are constant or
122  increasing (23).
123
124  Here, we perform trend analyses on a compiled NH dataset (1992-2022) of ambient $Hg^0$ measurements
125  and conduct biogeochemical box model and GEOS-Chem chemistry-transport model simulations to
126  identify emissions trends that would be compatible with observed concentration trends. We focus on $Hg^0$
127  measurements rather than gaseous oxidized mercury (GOM) and wet deposition measurements, as past
128  measurements of GOM may have been biased low (24) and wet deposition is more strongly affected by
129  meteorological variability (25). We derive trends not only in the mean or median changes in $Hg^0$, but also
130  in other statistical quantiles (e.g., 95th percentile) using quantile regression, which can provide additional
131  information regarding the drivers of trends.
132
133  **Results and Discussion**
134  **Regional trends in observed $Hg^0$ (1992–2022).** We analyzed $Hg^0$ data from 51 long-term monitoring
135  stations across the NH (Fig. 1). To calculate trends over wider regions, we aggregated stations based on
136  Intergovernmental Panel on Climate Change (IPCC) regions (26) and calculated overall trends using
137  linear mixed effect modeling (Fig. 2A–K and Table S1). Overall trends for all NH regions except
138  Northwestern North America are declining over the available measurement periods between 1992 and
139  2022, with declines ranging between -0.007 and -0.035 ng m$^{-3}$ yr$^{-1}$ (concentration units refer to standard
140  temperature and pressure, STP). Northwestern North America (Fig. 2J) is the only NH region to show a
141  positive trend, but this region only includes one measurement site (Little Fox Lake, Yukon, Canada). Two
142  possible hypotheses for the positive trend in Little Fox Lake have been suggested: increasing transport
143  from East Asia or increasing wildfire frequency in Western Canada (12). However, in our analysis, the
144  East Asian region also shows declining $Hg^0$ concentrations over 2006–2022 (trend -0.023 ± 0.005 ng m$^{-3}$
145  yr$^{-1}$) (Fig. 2H). Declines have also been observed in other published shorter term measurement records
146  from China (17, 18, 27, 28). For the regions with more available measurement stations, including Eastern
147  North America (ENA, n = 19) and Northern Europe (NEU, n = 13), we tested a nonlinear method of
148  obtaining an overall regional trend using generalized additive models (GAM) (8). The derived regional
149  trends are robust, as both the linear and nonlinear approaches of deriving regional trends yield similar
150  declines in these regions for 2005–2020 (-0.01 to -0.02 ng m$^{-3}$ yr$^{-1}$) (Supplemental Information, SI, Fig.

151   S4). We have also calculated similar regional trends when conducting a sensitivity test where the analysis
152   of site data is limited to the 2005–2020 period (SI Fig. S5 and Table S3).

154   We find an overall NH $Hg^0$ decline of -0.011 ± 0.006 ng m$^{-3}$ yr$^{-1}$ (± 2 standard deviations) for the period
155   2005–2020 (Fig. 2L), calculated by averaging regional trends (Fig. 2A–K) weighted by the areas of
156   corresponding IPCC regions. By first aggregating site trends by region, we reduce inherent biases from
157   the uneven spatial distribution of sites (i.e., biasing toward the trends of Eastern North America and
158   Europe) (SI Fig. S2). Our results largely agree with a previous trend assessment conducted on data from
159   1990–2014 (7), which found regional declines in $Hg^0$ of -0.6 to -2% yr$^{-1}$ (approximately corresponding to
160   -0.01 to -0.03 ng m$^{-3}$ yr$^{-1}$). The current work benefits from improved statistical techniques to combine
161   information from multiple sites and a larger number of stations and regions covered in more recent time
162   periods. We have not included an analysis of SH regional trends in the current work due to the sparse
163   coverage of SH long-term monitoring stations (Fig. 1). From published information, two SH monitoring
164   stations (Cape Point, South Africa and Amsterdam Island) do not show significant trends during the
165   2012–2017 period, while Cape Point shows a positive trend of ~0.008 ng m$^{-3}$ yr$^{-1}$ over 2007–2017 (19).
166   As the NH has a wider dataset of $Hg^0$ time series and is the principal hemisphere for anthropogenic
167   emissions, we proceed with constraining Hg budget trends based on the NH $Hg^0$ trend.

169   **Constraining emissions trends for 2005–2020**. We ran 2 × 10$^5$ scenarios in a biogeochemical box
170   model for 2005–2020, varying 19 Hg budget parameters including the trends in anthropogenic emissions
171   and releases, the response of legacy emissions to recent and historical anthropogenic inputs, emissions
172   speciation trends, and the atmospheric Hg lifetime (Table S4). Figure 3A compares the distributions of
173   simulated $Hg^0$ trends for specific trends in anthropogenic emissions, given the uncertainty ranges of all
174   other factors. Note that emissions fluxes are reported in Mg yr$^{-1}$, and thus trends in these fluxes are
175   expressed as Mg yr$^{-2}$. Our best estimate for the observed 2005–2020 trend in surface NH $Hg^0$ is -0.011 ±
176   0.006 ng m$^{-3}$ yr$^{-1}$. However, to account for potential differences between NH surface and whole
177   troposphere trends (SI Section S3.1) we assumed an extended uncertainty range for NH tropospheric $Hg^0$
178   trends from -0.017 to -0.004 ng m$^{-3}$ yr$^{-1}$ (error bar in Fig. 3A).

180   The uncertainty range for observed NH troposphere $Hg^0$ trends is compatible (>5% overlap in histogram)
181   only with anthropogenic emission trends that are declining by more than -9 Mg yr$^{-2}$ (Fig. 3A). Stronger
182   declines in anthropogenic emissions lead to more overlap between the simulated and observed trend
183   ranges, yet they become more difficult to reconcile with existing bottom-up inventories. Our box modeling
184   analysis is consistent with a previous emissions trend estimate based on 1990–2010 observations (610
185   Mg yr$^{-1}$ total difference; -30.5 Mg yr$^{-2}$ trend) (7). The positive NH anthropogenic emissions trend estimated
186   by the Streets et al. (10) inventory for 2005–2015 (34 Mg yr$^{-2}$), should result in NH $Hg^0$ increases on the
187   order of 0.09 ng m$^{-3}$ yr$^{-1}$, with no overlap in the observed trend range. Other global inventories differ in
188   terms of their temporal coverage, yet the EDGAR v4.tox2 inventory estimates an increase of 54 Mg yr$^{-2}$
189   over 2005–2012 in the NH (9) and the AMAP/UNEP inventory estimates an NH increase of 44 Mg yr$^{-2}$
190   between 2010 and 2015 (5). The EDGAR v8.1_toxHg inventory, which was recently released but remains
191   in draft form for speciation estimates (29), shows an NH increase of 35 Mg yr$^{-2}$ for 2005–2020 (Fig. S15),
192   We conclude that current bottom-up inventories of anthropogenic Hg emissions are inconsistent with the
193   declines in observed NH $Hg^0$ for 2005–2020.

195   Previous studies (21, 22) have hypothesized that NH $Hg^0$ may be decreasing due to broad-scale declines
196   in legacy emissions, even as anthropogenic emissions increase or stay constant. However, our
197   biogeochemical box model analysis illustrates that it is very unlikely for legacy emissions to decrease if
198   recent (2005–2020) anthropogenic emissions are not also decreasing. Even if anthropogenic emissions
199   stay constant, legacy emissions will grow due to the increasing supply of Hg (23). This effect means that

200    in the case of an anthropogenic emissions trend of zero, the median predicted $Hg^0$ trend will be positive
201    due to positive trends in re-emissions (Fig. 3A and Fig. S8B). The trend in anthropogenic emissions must
202    be below -8 Mg $yr^{-2}$ for the median predicted $Hg^0$ trend to become negative (Fig. S8B). We explored the
203    potential impacts of errors in the historical emission and release inventories on the recent re-emissions
204    trend (Fig. S9). If we assume underestimates in 1970 emissions and releases, when Hg discharges were
205    at their peak (30, 31), the recent re-emissions trend would be more negative (Fig. S9A). However, the
206    degree to which the potential error in 1970 emissions affects the 2005–2020 re-emissions trend is smaller
207    than the impacts of more recent errors (1990, 2000), and a factor of ~15 smaller than the influence of
208    contemporary (2005–2020) anthropogenic emissions and releases trends (Figs. S9F and G). Therefore,
209    although historical emissions and releases from earlier decades (>30 years) can affect the recent re-
210    emissions trend, the dominant factor for the recent re-emissions trend will be recent trends (<15 years) in
211    anthropogenic Hg inputs to the environment. Our results take into account the uncertainties in the multiple
212    lifetimes of legacy Hg in the surface environment (Table S4).

214    We explored the role of trend drivers other than anthropogenic inputs by repeating the sampling of the
215    box model throughout the parameter space, accounting for additional causes. If the oxidation lifetime of
216    $Hg^0$ declined between 2005–2020, it can become easier to reconcile the observed $Hg^0$ decline with
217    positive anthropogenic emissions trends (Fig. 3B). However, the oxidation lifetime of $Hg^0$ would have to
218    decline by 13% for at least a 5% likelihood of positive anthropogenic emissions trends (i.e., when the
219    oxidation lifetime declines by 13% over 2005–2020, 5% of the simulations that are within the observed
220    NH $Hg^0$ trend range have positive NH anthropogenic emissions trends). A hemispheric decrease in the
221    oxidation lifetime of this magnitude would be surprising for the 2005–2020 period, as modeling estimates
222    for the methane ($CH_4$) lifetime suggest only 9% declines over the longer period of 1980–2014, driven by
223    increases in hydroxyl radical (OH) concentrations (32). In addition, the two-step Hg oxidation chemistry
224    will be affected by other oxidants as well, including ozone, bromine radicals, and nitrogen oxides (2, 33–
225    35). A recent study has highlighted the role of anthropogenic short-lived halogens in continental Hg
226    oxidation, with more work required to understand their trends (36). Oxidants impacted by anthropogenic
227    pollution sources have likely trended differently in different regions, and therefore are likely not the main
228    factor between the consistent $Hg^0$ declines seen across the NH. In the unlikely scenario that increased
229    $Hg^0$ oxidation rates counteracted constant or increasing anthropogenic emissions to yield negative $Hg^0$
230    trends, one would still expect to see a positive trend in NH Hg wet deposition. This is because: 1) larger
231    emissions would need to be balanced by larger deposition fluxes; and 2) the accelerated oxidation of $Hg^0$
232    would lead to more Hg depositing through wet deposition (the major fate of soluble $Hg^{II}$) rather than dry
233    deposition of $Hg^0$. However, previous studies have identified overall declines in wet deposition of Hg over
234    North America (13, 14, 37) and Europe (5).

236    Another potential factor is the increase in terrestrial primary production through global greening, which
237    Jiskra et al. (20) estimated increased the NH dry deposition of $Hg^0$ to vegetation by 140 Mg $yr^{-1}$ between
238    1990 and 2010; this corresponds to a decrease of approximately 13% in their estimated $Hg^0$ lifetime due
239    to vegetation uptake. However, the NH $Hg^0$ dry deposition lifetime would have to decline by more than
240    19% between 2005 and 2020 to yield a 5% likelihood of positive anthropogenic emissions trends (Fig.
241    3C). A change of this magnitude to vegetation uptake during 2005–2020 is unrealistic, as our GEOS-
242    Chem simulation for that time period shows only a 3% decline in the $Hg^0$ dry deposition lifetime due to
243    vegetation changes (Fig. S11). Other climate change factors can play a role in recent legacy emissions
244    trends, like release of Hg from melting permafrost (38), changes to ocean evasion of $Hg^0$ through
245    warming, acidification, and wind speed changes (39), decreased sea ice coverage allowing further $Hg^0$
246    evasion (40), and enhanced wildfire emissions (41). These identified climate feedbacks, however, tend to
247    increase legacy Hg re-emissions, and thus could not explain why anthropogenic emissions in bottom-up
248    inventories increase while $Hg^0$ trends decline. Although further research into these factors is required to

249 reduce uncertainties in recent trend drivers, our conclusion remains that it is very unlikely that NH
250 anthropogenic emissions could have increased or even stayed constant over 2005–2020, with the $Hg^0$
251 declines observed over this period in the NH.
252
253 **Spatial and quantile variability of $Hg^0$ trends.** Although the box model is useful for constraining overall
254 hemispheric trends, it cannot capture the spatial heterogeneity of these trends driven by variability in
255 sources, sinks, and transport. As these simulations are run with observed meteorology from the MERRA-
256 2 reanalysis product (42), the GEOS-Chem simulations account for interannual variability or potential
257 climate change-driven trends in meteorology for 2005–2020. We ran simulations (Table 1) in the 3-D
258 chemical-transport model GEOS-Chem (43, 44) to investigate different emissions scenarios over the
259 2005–2020 period and calculated mean trends in NH $Hg^0$ using area-weighted averaging of observed
260 regions (Fig. 4A). The BASE simulation, including anthropogenic emissions increases according to
261 Streets et al. (10) for 2005–2015 with constant emissions after 2015, shows an increase in NH $Hg^0$ of
262 0.006 ng $m^{-3}$ $yr^{-1}$. In the BASE+LEG simulation, we considered the feedback of legacy emissions to
263 increasing anthropogenic emissions, leading to a stronger increase of 0.010 ng $m^{-3}$ $yr^{-1}$ in NH $Hg^0$.
264 Echoing the box modeling results, we thus find that increases in anthropogenic emissions found in
265 existing inventories is inconsistent with the observed trends in NH $Hg^0$, -0.011 ± 0.006 ng $m^{-3}$ $yr^{-1}$.
266 Replacing Chinese emissions within BASE by the regional inventory trend from Zhang et al. (45), the
267 ZHANG23 simulation shows a slight negative trend in NH $Hg^0$ (-0.001 ng $m^{-3}$ $yr^{-1}$). We simulated two
268 further scenarios for a decreasing NH emissions trend: DEC_ANT_NH, where an additional decline of 23
269 Mg $yr^{-2}$ in the NH is imposed on top of the ZHANG23 scenario, and DEC_LEG_ONLY, which considers
270 declining ocean re-emissions of Hg in the NH and SH. Both of these emission scenarios are within
271 uncertainties of the observed trend in mean NH $Hg^0$ (DEC_ANT_NH: -0.009 ng $m^{-3}$ $yr^{-1}$;
272 DEC_LEG_ONLY: -0.012 ng $m^{-3}$ $yr^{-1}$). Since it is difficult to understand the causes of the $Hg^0$ decline
273 based on the mean hemispheric trend alone, we also assess the spatial and quantile variations in trends.
274
275 We use quantile regression to assess trends in the observed median (P50) and 95th percentile (P95)
276 deseasonalized daily $Hg^0$ values. Fig. 4B maps the simulated P50 trends in BASE+LEG, showing
277 increasing concentrations across the globe, in disagreement with 8 of the 9 plotted stations (>13 years
278 observed between 2005 and 2020), which show declines. The difference between P95 trends and P50
279 trends (Fig. 4C) correlates with the change in anthropogenic emissions between 2005 and 2020 (Fig.
280 S12). BASE+LEG simulates P95 declining more than P50 in Eastern North America and Central Europe
281 (areas of emissions decreases in the global inventory), while P95 increases more than P50 in East Asia
282 and South Africa (areas of emissions increases). Available high-resolution measurement records confirm
283 the simulated P95 – P50 trends in Eastern North America (Egbert and Kejimkujik) and Europe (Mace
284 Head, Schmücke, and Pallas), yet they also show declines in East Asia (Cape Hedo). In the simulations
285 where Chinese emissions decline between 2005 and 2020 (ZHANG23 and DEC_ANT_NH), the
286 simulated P95 – P50 trends agree with observations at Cape Hedo, showing negative values (Figs. 4E
287 and S12D). In the DEC_LEG_ONLY simulation, declining legacy emissions lead to agreement with the
288 observed P50 NH $Hg^0$ trends (Fig. 4F), but the P95 – P50 trends remain similar to BASE+LEG and are
289 opposite in sign to Cape Hedo observations (Fig. 4G). Therefore, despite showing similar P50 trends
290 (Figs. 4D and F) in NH $Hg^0$, DEC_ANT_NH and DEC_LEG_ONLY can be distinguished by simulated
291 patterns in quantile trends. The current results support findings from Hg measurement studies in the
292 1990s (46, 47), which suggested that reductions in observed extreme concentrations could be useful
293 indicators for regional emissions changes. Incorporation of quantile trends as constraints in Hg modeling
294 can thus help maximize the information provided by high resolution monitoring stations.
295
296
297

298 **Implications for the drivers of atmospheric Hg trends.**
299 Observed $Hg^0$ is generally declining in most NH regions, with an estimated hemispheric trend of -0.011 ±
300 0.006 ng $m^{-3}$ $yr^{-1}$ for 2005–2020. By testing a large ensemble of parameters using box modeling and
301 comparing with available measurements of atmospheric concentrations, we showed that NH
302 anthropogenic emissions likely declined by more than -140 Mg $yr^{-1}$ (-9 Mg $yr^{-2}$) over this period (Fig. 3A).
303 This result is at odds with existing anthropogenic emissions inventories (5, 9, 10, 29), which all show NH
304 increases of larger than 34 Mg $yr^{-2}$. Thus, there is a potential gap of 43 Mg $yr^{-2}$ (~650 Mg $yr^{-1}$) between
305 estimated anthropogenic emissions trends from inventories and trends expected from observed $Hg^0$
306 trends. This gap could quantitatively be impacted (in both directions) by factors like the $Hg^0$ oxidation
307 lifetime and vegetation sink, yet it is unlikely to be substantially reduced (Fig. 3B–C). Our ZHANG23
308 simulation showed that this gap could be partially explained by incorrect Chinese emissions trends in the
309 global emission inventory, with Chinese national inventories including more detailed information on air
310 pollution control device efficiencies (45, 48, 49). The hypothesis of declining Chinese emissions is
311 supported by the observed decline in P95 $Hg^0$ concentrations at Cape Hedo (Fig. 4E), along with
312 observed declines in mean $Hg^0$ values from other East Asian stations (Fig. 2H). However, additional
313 declines in anthropogenic emissions across the NH were necessary to match the magnitude of the
314 observed trend in the DEC_ANT_NH simulation. The gap between inventories and measurement-derived
315 emissions trends could be due to the large uncertainties associated with several anthropogenic emissions
316 sources. For example, ASGM is currently thought to be the largest yet highly uncertain source (globally
317 775 Mg $yr^{-1}$ in 2015) of anthropogenic Hg emissions (10), and estimated trends in this source can differ
318 depending on whether it is estimated to change with time following different proxies such as gold demand
319 or poverty (10, 50). High uncertainties are also linked with emissions from Hg-containing products
320 (globally 436 Mg $yr^{-1}$) (10), as the magnitudes of historically produced Hg are large (~1000 Gg) and
321 emissions factors as well as timescales are uncertain (51). Measurement constraints are limited, and our
322 five tested GEOS-Chem simulations are not intended to cover the entire range of uncertainty in emissions
323 scenarios, so we cannot further identify the source types responsible for the discrepancy between
324 emissions inventory and observed trends. Nevertheless, both our box and GEOS-Chem modeling
325 analyses suggest that a decline in legacy emissions in the absence of anthropogenic emissions
326 reductions is unlikely given our understanding of the Hg cycle and measured quantile trends.
327
328 The amount of uncertainty in anthropogenic emissions and biogeochemical cycling of Hg emphasizes the
329 need for continued assessment of inventories and models based on available observations and emerging
330 constraints like Hg isotopes (52). Expansion of current monitoring networks in strategic locations and
331 increased public availability of data would be valuable for trend quantification and attribution to sources.
332 For example, existing SH measurement locations are largely influenced by marine rather than
333 anthropogenic sources (53, 54), with no long-term measurement stations located nearby ASGM activities
334 (Fig. 1). We focused here on trends in $Hg^0$ in the NH due to the increased prevalence of NH
335 anthropogenic emissions and monitoring, but further monitoring of atmospheric Hg in the SH is essential
336 for constraining trends in Hg sources. For example, major differences between the simulated
337 DEC_ANT_NH and DEC_LEG_ONLY median trends occur in the SH (Fig. 4), but we do not evaluate the
338 accuracy of the simulated SH trends as analysis of SH measurements is out of the scope of the current
339 study. Passive samplers (55) can enable economical Hg monitoring in remote locations, yet active
340 continuous sampling will continue to deliver the benefits of higher time resolution (e.g., atmospheric
341 dynamics, source identification) compared to passive samplers (~monthly resolution). Here we showed
342 that the trends in the statistical distribution of $Hg^0$, which can only be facilitated by active sampling
343 methods, are a useful indicator of which sources are changing. As more data become available from sites
344 measuring GOM using a new generation of methods with smaller biases (56, 57), it will be possible to
345 analyze long term trends in different fractions of atmospheric Hg, providing further information about
346 source changes. Reduced-form models (58, 59) and tools to produce emissions inventories from

347 socioeconomic data more quickly (60), which have been applied extensively in the climate and air
348 pollution fields, can enable more up-to-date evaluations of the latest Hg trends and drivers. Improvements
349 in Hg models will be essential for further analysis of Hg trends, for example refining the response of
350 legacy re-emissions to anthropogenic emissions scenarios and global change factors. The planned
351 analysis to support the Minamata Convention effectiveness evaluation will advance this approach by
352 investigating the drivers of Hg trends in multiple Hg models (61). As declining atmospheric Hg inputs to
353 ecosystems can directly impact concentrations of Hg in biota (62), understanding the trends in
354 atmospheric Hg burden is essential for better predictions of how Hg pollution will evolve under future
355 regulatory control scenarios and climate change.
356
357 **Materials and Methods**
358 **Atmospheric mercury observations.** Atmospheric mercury (Hg) occurs as different species: the volatile
359 species gaseous elemental mercury (GEM: $Hg^0$), the soluble, shorter-lived species gaseous oxidized
360 mercury (GOM: $Hg^I$ and $Hg^{II}$), and particulate-bound mercury ($Hg^P$). We compiled data from 51 stations
361 which have more than 6 years of measurements of $Hg^0$ or total gaseous mercury (TGM = $Hg^0$ + GOM) in
362 the period 1992 to 2022 (Table S1). Measurements reporting TGM are likely more representative of $Hg^0$
363 due to low biases in capturing GOM (63, 64), and therefore we do not differentiate between TGM and $Hg^0$
364 measurements. For the main manuscript analysis, we compare modeled $Hg^0$ quantities to the combined
365 TGM and $Hg^0$ measurement dataset. As a sensitivity test, we excluded all TGM measurements from the
366 datasets, but found no significant differences in regional trends when analyzing $Hg^0$ measurements alone
367 (Section S4, Fig. S6). We have also tested whether the trend results are similar if modeled TGM data are
368 analyzed instead of modelled $Hg^0$ and the differences are minor (< 0.001 ng $m^{-3}$ $yr^{-1}$). We analyzed data
369 from multiple measurement networks: the US National Atmospheric Deposition Program's (NADP)
370 Atmospheric Mercury Network (AMNet) (65), Environment and Climate Change Canada's network
371 (ECCC) (37), European Monitoring and Evaluation Programme (EMEP) (66), Global Mercury Observation
372 System (GMOS) (67), Ministry of Environment Japan (MOEJ) (15), Ministry of Environment (MOENV)
373 Taiwan (16), and the Experimental Lakes Area (68). We also included a Mauna Loa measurement
374 dataset from the US EPA from 2002 to 2009 (69, 70), which later transitioned into an AMNet site. Most
375 TGM and $Hg^0$ measurements were made with Tekran Instruments Corporation (Toronto, Canada) Models
376 2537A/B/X systems, which capture ambient Hg by gold trap amalgamation, subsequently thermally
377 desorbing this accumulated Hg to be detected by Cold Vapour Atomic Fluorescence Spectrometry
378 (CVAFS) (70). Two sites in the EMEP network (Iskrba after 2017 and Lahemaa) employed Lumex
379 Instruments (St. Petersburg, Russia) Model RA-915 mercury analyzers, which detect $Hg^0$ through
380 Zeeman Atomic Absorption Spectrometry using High Frequency Modulated light polarisation (ZAAS-HFM)
381 (71). Before 2017, TGM was measured at Iskrba with Mercury Instruments Analytical Technologies
382 (Karlsfeld, Germany) Model UT-3000 analyzers using cold vapor atomic absorption spectroscopy
383 (CVAAS). All the continuous TGM and $Hg^0$ measurements are made at 5–15 min intervals, which are
384 averaged and reported hourly. Measurements from Zeppelin Station (before 2000), Birkenes (before
385 2010), Lista, Råö, Bredkälen, Hallahus, and Pallas (the measurements from IVL, Swedish Environmental
386 Research Institute) were made manually with a gold trap sampling technique (72). Data at lower
387 frequencies (manual sites and the Auchencorth Moss and Iskrba timeseries) were used to compute
388 monthly mean statistics for timeseries. At the sites with high-frequency measurements, daily mean values
389 were calculated and used to compute means for all months with at least 10 daily values. All measurement
390 and modeling data for $Hg^0$ is reported in units of ng $m^{-3}$ $yr^{-1}$ at standard temperature and pressure (STP, 0
391 °C and 1 atm).
392
393 **Statistical methods.** Monthly mean data were deseasonalized before trend analysis by fitting each
394 station timeseries with four harmonic terms (73). In order to achieve a better evidence synthesis from
395 individual site data, we focused our statistical analysis on calculating overall trends from wider regions.

396 We chose to aggregate Hg trends based on the IPCC regions (Fig. 1). These regions are standardly used
397 in the atmospheric science community and are designed to have consistent climate features (26),
398 providing advantages over using whole continent or country-based aggregations. There are 61 regions in
399 total; we analyzed trends for 11 regions in the NH where stations measuring Hg over the long term (> 6
400 years) were available. We aim to derive regionally representative trends by integrating information from all
401 data sources, because individual sites might only provide a partial view of regional variations, as they
402 cover different time periods, come from different measurement networks, include data gaps, and are
403 potentially exposed to unique local sources and sinks. In previous studies on Hg trends, regional
404 timeseries have been calculated by averaging all sites that are available in a particular year (7). However,
405 this approach is biased when sites do not all cover the same time period, since offsets between mean site
406 concentrations can affect the calculated trend results (SI Section S3.2). To address this heterogeneity, we
407 explicitly modeled offsets and trend deviations between sites with linear mixed effects (LME) models (73,
408 74). Using LME models, a time series can be described with terms representing the consensus trend and
409 intercept for a region ("fixed effect") and terms representing site-level deviations ("random effect").
410 Individual sites were modeled using Eq. 1:

$$y_k = a + bt + \alpha_k + \beta_k t \qquad \text{(Eq. 1)}$$

412 where $y_k$ are deseasonalized monthly mean $Hg^0$ values for each site, $a$ is the regional intercept, $b$ is the
413 regional trend, $a_k$ is the site offset, and $\beta_k$ is the site deviation in trend. To account for autocorrelation, we
414 assumed that residual errors for each site follow a first-order autoregressive process (AR(1)). We
415 calculated these trends using LME modeling in the R package lme4 (74). For the purposes of LME
416 modeling, EPA and AMNet data for Mauna Loa, as well as Finnish Meteorological Institute (FMI) and
417 Swedish Environmental Research Institute (IVL) data for Pallas, were treated as different sites (as
418 different measurement networks may have offsets). We applied LME modeling to the nine NH regions
419 where multisite data is available. For the two regions (Northwestern North America and the Arctic Ocean)
420 where only one site is available, we calculated generalized least squares (GLS) trends with AR(1) errors
421 on deseasonalized monthly mean values. We chose linear approaches for trend analysis as this follows
422 recommendations for multisite analysis when only a few sites are available for a region (73). We found
423 consistent results between LME trends and nonlinear trends calculated with generalized additive models
424 (GAMs) for regions (Eastern North America and Northern Europe) where a larger number of sites (>12)
425 are available (SI Fig. S4).

426

427 We weighted regional trends by the areas of the corresponding IPCC regions to calculate the overall NH
428 trend, which allowed us to compare with box model simulations. The overall NH trend was calculated for
429 2005–2020, which is the time period with the best availability of data from all 11 regions. The error in the
430 NH trend was calculated through Monte Carlo sampling of regional trends ± 2 standard deviation.
431 Analogous trend calculations were performed for GEOS-Chem simulated $Hg^0$ values, which showed that
432 NH trends derived from regional weighted averages were more representative of the true NH surface
433 trend than averages of all available sites without regional aggregation (SI Fig. S2).

434

435 For sites where high frequency $Hg^0$ measurements were available, we additionally calculated quantile
436 regression (QR) trends over the 2005–2020 period (75). Other atmospheric chemistry studies (8, 76, 77)
437 have applied QR, as it enables the quantification of trends not only in the mean values but throughout the
438 distribution of the observed quantity. Earlier studies have observed heterogeneous changes in the
439 statistical distribution of atmospheric Hg measurements driven by emissions changes (46, 47), yet these
440 have not been followed up with more modern statistical techniques. We analyzed deseasonalized daily
441 mean values at these sites and calculated trends for $5^{th}$–$95^{th}$ percentiles, with errors derived using
442 bootstrapping. We applied the R package quantreg for this analysis (78).

443

444  **Box model simulations.** We used a 3-box model that considers atmospheric $Hg^0$ and $Hg^{II}$ in two
445  tropospheric boxes (NH and SH) and one stratospheric box (79) to simulate potential scenarios for trends
446  during 2005–2020. We constructed an ensemble of scenarios accounting for uncertainties in the
447  atmospheric Hg lifetime, historical (pre-2005) anthropogenic emissions and releases, recent (2005–2020)
448  anthropogenic emissions and releases, the response of legacy emissions to anthropogenic inputs, and
449  recent (2005–2020) speciation trends. We assigned uncertainty ranges to these 19 parameters (SI Table
450  S4) and sampled $2 \times 10^5$ scenarios within this parameter space, using Latin Hypercube Sampling (80).
451
452  To address the response in legacy emissions to historical and recent anthropogenic inputs, we applied
453  the effective anthropogenic mercury deposition (EAMD) concept (81). Our approach used two minor
454  adaptations: (1) tracking the effective anthropogenic mercury emissions (EAME) instead of deposition
455  (which leads to offsets of several months in lifetimes); and (2) using a two-term negative exponential
456  model. Given primary emissions or releases of mercury in a specific year ($\epsilon_i$), Eq. 2 calculates the EAME,
457  in a future time $t$:

$$\text{EAME}_i\,(t) = \epsilon_i \left( a_1 \exp\left(-\frac{t}{b_1}\right) + a_2 \exp\left(-\frac{t}{b_2}\right) \right) \qquad \text{(Eq. 2)}$$

460  where $a_1$ and $a_2$ are coefficients and $b_1$ and $b_2$ are lifetimes representing the quick and slow re-emission
461  processes, respectively. Total legacy emissions ($E_{\text{leg}}$) in the year $t$ were calculated by summing up all
462  $\text{EAME}_i$ resulting from previous primary emissions using Eq. 3:

$$E_{\text{leg}}\,(t) = \sum_{i<t} \text{EAME}_i \qquad \text{(Eq. 3)}$$

466  We employed pulse experiments with parameter perturbations in the Hg Global Biogeochemical Box
467  model (GBC) (6, 82) to calculate reasonable ranges for the $a$ and $b$ parameters (SI Section S5). We
468  pulsed an additional 100 Mg Hg either emitted or released to rivers in 2010 and fit the resultant additional
469  legacy re-emissions until 2110 using Eq. 2. We conducted these pulse experiments on 1000 iterations of
470  the GBC model, varying each of the 40 rate coefficients and parameters within the GBC model within a
471  factor of 2 using Latin Hypercube Sampling. We found that $b_1$ ranges between 6–15 months for
472  atmospheric emissions and 2–10 months for releases, corresponding to the timescale of atmospheric
473  deposition and re-emission from the surface ocean. The longer lifetime, $b_2$, ranges between 29–97 years
474  for atmospheric emissions and 1–117 years for releases, corresponding to the timescale of removal of Hg
475  from the atmosphere–surface ocean–subsurface ocean system through transfer to the deep ocean or
476  temporary storage in soils (6). We calculated ranges for the fraction of Hg re-emitted in the short
477  timescale term and the total Hg re-emissions resulting from a pulse, which can be used to calculate $a_1$
478  and $a_2$ in Eq. 2. Although longer time scales (~1000 yr) would be required to model burial of Hg in the
479  deep ocean, Eq. 2 covers the legacy re-emission response in near-future projections (<100 years), while
480  having only 4 parameters as opposed to 40 parameters in the GBC model (81).
481
482  Anthropogenic emissions and releases of Hg were taken from the Streets et al. (31) inventory, which
483  covers decadal points over the historical period (1510–2010). We accounted for uncertainties in
484  emissions and releases for recent decadal points (1970, 1980, 1990, 2000, 2010) by applying
485  perturbations between –20% and +40% to these values, which is the suggested emission inventory
486  uncertainty range (10). We interpolated between the decadal points to calculate emissions with yearly
487  resolution between 1510–2005. For 2005–2020, we applied varying linear trends in anthropogenic
488  emissions for both hemispheres, restricting the trend range to ensure non-negative emissions in 2020.
489  The anthropogenic releases for 2005–2020 were calculated based on the historical relationship between
490  emissions and releases trends in the inventory (31), with random perturbations introduced for the
491  hemispheric release trends (Table S4). This procedure yielded $2 \times 10^5$ potential timeseries for

492  anthropogenic emissions and releases over 1510–2020. Combining these scenarios with varying sets of
493  legacy parameters (Eq. 2), we calculated the resultant global legacy re-emissions timeseries for 2005–
494  2020 for each of the $2 \times 10^5$ scenarios. For simplicity, the distribution of legacy re-emissions by
495  hemisphere was assumed to be constant over 2005–2020 based on the ratio in GEOS-Chem (44% NH,
496  55% SH; this is similar to the ratio of ocean coverage in the NH and SH). Speciation of the anthropogenic
497  emissions in 2005 was set to 65% $Hg^0$ and 35% $Hg^{II}$; we applied a variable linear trend in speciation so
498  that speciation in 2020 ranged between 45% and 85% $Hg^0$.

500  We ran the $2 \times 10^5$ scenarios in the 3-box model for 2005 to evaluate whether the sampled combinations
501  of emissions and atmospheric Hg lifetimes (ranging between 3–8 months) yield a reasonable Hg burden.
502  We rejected scenarios that yield a 2005 burden in the NH troposphere outside of the range 1600–3300
503  Mg (corresponding to average tropospheric concentrations of 0.8–1.6 ng m$^{-3}$). Approximately $10^5$ samples
504  passed this constraint, which we then utilized for full 2005–2020 box model runs. We evaluated linear
505  trends in NH $Hg^0$ in each of these box model runs and compared these to the inputted total and
506  anthropogenic emission trends for 2005–2020.

508  To assess the impacts of other non-emissions factors in NH $Hg^0$ trends, we repeated this procedure
509  accounting for potential trends in $Hg^0$ dry deposition and oxidation. We re-ran the $2 \times 10^5$ scenarios with
510  linear trends in the dry deposition rate coefficient so that the value in 2020 varied between 100% to 170%
511  of its value in 2005. Similarly, we ran $2 \times 10^5$ scenarios with the $Hg^0$ oxidation rate coefficient varying in
512  2020 between 100% and 200% of its value in 2005.

514  **GEOS-Chem simulations.** We ran 3-D atmospheric simulations for the 2005–2020 period in the
515  chemistry-transport model GEOS-Chem. We used version 12.8.1 of the Hg model (43) with improvements
516  in the dry deposition of $Hg^0$ (79). The model was run globally at 2.0° × 2.5° horizontal resolution and 47
517  vertical levels up to 0.01 hPa (80 km). The model was forced with offline meteorology from the MERRA-2
518  product (42). The model treats three species of Hg: elemental mercury ($Hg^0$), oxidized mercury ($Hg^{II}$,
519  GOM), and particulate mercury ($Hg^P$). Oxidation of $Hg^0$ occurs through a two-step mechanism initiated by
520  atomic bromine (Br), while photoreduction of $Hg^{II}$ occurs in the aqueous phase as a function of the $NO_2$
521  photolysis rate and organic aerosol concentrations (43). The reduction rate coefficient (K_RED_JNO2)
522  was set to 2.4 m$^{-3}$ µg$^{-1}$ so that modeled $Hg^0$ concentrations agree with observed values in 2005. The Hg
523  chemistry in GEOS-Chem has been updated in more recent model versions (v14 onwards), yet the
524  overall atmospheric lifetime and transport of Hg remain similar (2) and the faster computational speed of
525  v12.8.1 facilitates these 16-year simulations. Legacy re-emissions of Hg from the ocean are calculated
526  online (depending on temperature and wind speed) through an air-sea exchange parametrization (83),
527  with concentrations of Hg in the surface ocean taken from a previous ocean general circulation model
528  (MITgcm) simulation (43). Soil legacy emissions are parametrized depending on solar radiation,
529  vegetation cover, and concentrations of Hg in soil (84). The model also considers prompt recycling of $Hg^{II}$
530  deposited to soils and snow (85), geogenic emissions of $Hg^0$ (44), and transient emissions of $Hg^0$ from
531  biomass burning based on GFED v4.1s (86). More comprehensive descriptions of this version of the
532  GEOS-Chem Hg model can be found elsewhere (43, 79).

534  Five simulations (Table 1) were performed to evaluate spatial heterogeneity in atmospheric Hg trends
535  under different emissions scenarios (SI Fig. S10), which are intended to be illustrative but do not cover
536  the full range of potential scenarios. The BASE case used Streets et al. (10) anthropogenic emissions of
537  Hg for 2005–2015, with 2016–2020 retaining the same emissions pattern as 2015. The BASE+LEG
538  simulation additionally considered the median box modeled trend (Fig. S9F) in NH legacy emissions (+14
539  Mg yr$^{-2}$) due to the BASE trend in NH anthropogenic emissions (+23 Mg yr$^{-2}$) over 2005–2020. This trend
540  in legacy emissions was fully ascribed to the ocean through scaling oceanic sea surface concentrations of

541 Hg (43) to yield the NH trend in legacy emissions. In the ZHANG23 scenario, we replaced the trend in
542 Chinese emissions from BASE with the national inventory in Zhang et al. (45). To distribute Chinese
543 emissions in a consistent way with the Streets et al. (10) inventory, we scaled the emissions for 2005–
544 2020 using the equation:
545

$$E_{\text{ZHANG23}}^{i'} = E_{\text{BASE}}^{i} \times \frac{E_{\text{ZHANG23}}^{i}}{E_{\text{ZHANG23}}^{2005}} \qquad \text{(Eq. 4)}$$

547

548 where $E_{\text{ZHANG23}}^{i'}$ are the distributed Chinese emissions applied in the ZHANG23 simulation for year $i$,
549 $E_{\text{BASE}}^{i}$ are the Chinese emissions applied in the BASE, $E_{\text{ZHANG23}}^{i}$ are the total Chinese emissions for a
550 specific year in the Zhang et al. (45) inventory, and $E_{\text{ZHANG23}}^{2005}$ are the total Chinese emissions in the Zhang
551 et al. (45) inventory for 2005. In this way, the normalized China trend for 2005–2020 is taken from the
552 Zhang et al. (45), but emissions magnitudes differ due to differences in 2005 total Chinese emissions
553 between BASE (701 Mg yr$^{-1}$) and Zhang et al. (45) (466 Mg yr$^{-1}$). We also adjusted the ZHANG23 trend in
554 NH legacy emissions (+4 Mg yr$^{-2}$) by scaling ocean concentrations so that it is coherent with the NH
555 anthropogenic emissions trend (-11 Mg yr$^{-2}$) (Fig. S9F).
556

557 To develop a scenario with declining anthropogenic emissions that would be compatible with observed
558 NH Hg$^0$ trends (DEC_ANT_NH), we imposed an additional 23 Mg yr$^{-2}$ decline for 2005–2020 in the NH.
559 Anthropogenic Hg emissions outside of China were scaled uniformly by year so that the decline is 23 Mg
560 yr$^{-2}$ more than in ZHANG23, for a total anthropogenic trend of -34 Mg yr$^{-2}$ (Table 1). NH legacy emissions
561 (-2 Mg yr$^{-2}$) were adjusted to be consistent with the DEC_ANT_NH trend in anthropogenic emissions. As
562 a fifth scenario, we explored the possibility where anthropogenic emissions follow BASE, but a major
563 decline (-50 Mg yr$^{-2}$) in NH ocean legacy emissions occurs (DEC_LEG_ONLY). Thus, the mean NH
564 trends in Hg$^0$ are similar between DEC_ANT_NH and DEC_LEG_ONLY (Fig. 4A), but the source
565 contribution and spatial distribution varies. In addition, while DEC_ANT_NH includes stagnant overall SH
566 emissions (-2 Mg yr$^{-2}$), DEC_LEG_ONLY has SH emissions declines (-74 Mg yr$^{-2}$) due to the scaling of
567 ocean concentrations.
568

592     **Code and Data Availability**
593     Model code, analysis scripts, and all data to reproduce figures and analyses are published in Zenodo
594     (https://doi.org/10.5281/zenodo.13618039) under a CC BY 4.0 license
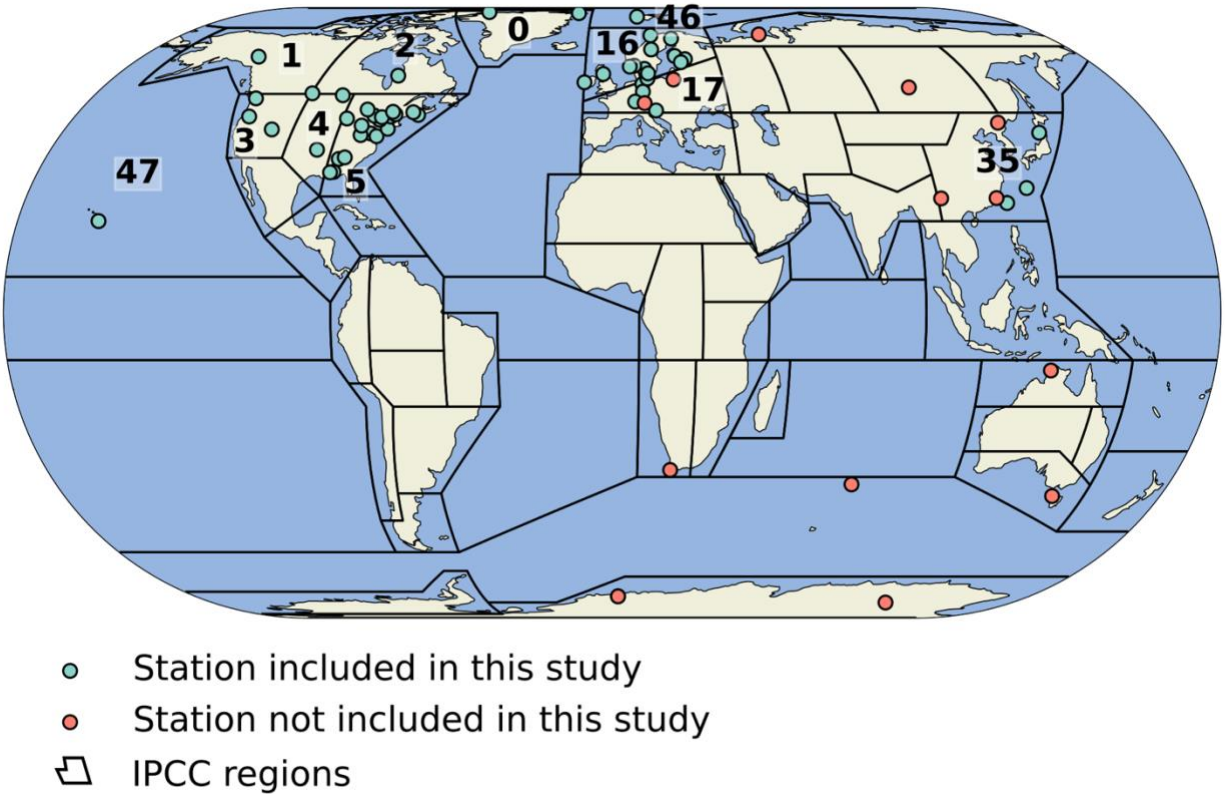595     (https://creativecommons.org/licenses/by/4.0/).
596

**References**

1. UNTC, Minamata Convention on Mercury (2013).
2. V. Shah, *et al.*, Improved Mechanistic Model of the Atmospheric Redox Chemistry of Mercury. *Environ. Sci. Technol.* **55**, 14445–14456 (2021).
3. UNEP/MC/COP.3, "Proposed indicators for evaluating the effectiveness of the Minamata Convention, by article. Annex I to decision MC-3/10." (2020).
4. F. Steenhuisen, S. J. Wilson, Development and application of an updated geospatial distribution model for gridding 2015 global mercury emissions. *Atmos. Environ.* **211**, 138–150 (2019).
5. UNEP, *Global Mercury Assessment 2018* (UN Environment Programme, Chemicals and Health Branch. Geneva, Switzerland, 2019).
6. H. M. Amos, D. J. Jacob, D. G. Streets, E. M. Sunderland, Legacy impacts of all-time anthropogenic emissions on the global mercury cycle. *Global Biogeochem. Cycles* **27**, 410–421 (2013).
7. Y. Zhang, *et al.*, Observed decrease in atmospheric mercury explained by global decline in anthropogenic emissions. *Proc. Natl. Acad. Sci. U.S.A.* **113**, 526–531 (2016).
8. K.-L. Chang, *et al.*, Trend detection of atmospheric time series. *Elementa: Science of the Anthropocene* **9**, 00035 (2021).
9. M. Muntean, *et al.*, Evaluating EDGARv4.tox2 speciated mercury emissions ex-post scenarios and their impacts on modelled global and regional wet deposition patterns. *Atmospheric Environment* **184**, 56–68 (2018).
10. D. G. Streets, *et al.*, Global and regional trends in mercury emissions and concentrations, 2010–2015. *Atmospheric Environment* **201**, 417–427 (2019).
11. D. Custódio, *et al.*, Odds and ends of atmospheric mercury in Europe and over the North Atlantic Ocean: temporal trends of 25 years of measurements. *Atmos. Chem. Phys.* **22**, 3827–3840 (2022).
12. K. MacSween, *et al.*, Updated trends for atmospheric mercury in the Arctic: 1995–2018. *Science of The Total Environment* **837**, 155802 (2022).
13. C. I. Olson, H. Fakhraei, C. T. Driscoll, Mercury Emissions, Atmospheric Concentrations, and Wet Deposition across the Conterminous United States: Changes over 20 Years of Monitoring. *Environ. Sci. Technol. Lett.* **7**, 376–381 (2020).
14. P. S. Weiss-Penzias, *et al.*, Trends in mercury wet deposition and mercury air concentrations across the U.S. and Canada. *Science of The Total Environment* **568**, 546–556 (2016).
15. K. Marumoto, *et al.*, Long-Term Observation of Atmospheric Speciated Mercury during 2007–2018 at Cape Hedo, Okinawa, Japan. *Atmosphere* **10**, 362 (2019).
16. L. S. P. Nguyen, G.-R. Sheu, D.-W. Lin, N.-H. Lin, Temporal changes in atmospheric mercury concentrations at a background mountain site downwind of the East Asia continent in 2006–2016. *Science of The Total Environment* **686**, 1049–1056 (2019).
17. J. Shi, *et al.*, Measurement report: Atmospheric mercury in a coastal city of Southeast China – inter-annual variations and influencing factors. *Atmos. Chem. Phys.* **22**, 11187–11202 (2022).
18. Q. Wu, *et al.*, Developing a statistical model to explain the observed decline of atmospheric mercury. *Atmospheric Environment* **243**, 117868 (2020).
19. F. Slemr, *et al.*, Atmospheric mercury in the Southern Hemisphere – Part 1: Trend and inter-annual variations in atmospheric mercury at Cape Point, South Africa, in 2007–2017, and on Amsterdam Island in 2012–2017. *Atmos. Chem. Phys.* **20**, 7683–7692 (2020).
20. M. Jiskra, *et al.*, A vegetation control on seasonal variations in global atmospheric mercury concentrations. *Nature Geosci* **11**, 244–250 (2018).
21. F. Slemr, E.-G. Brunke, R. Ebinghaus, J. Kuss, Worldwide trend of atmospheric mercury since 1995. *Atmos. Chem. Phys.* **11**, 4779–4787 (2011).
22. A. L. Soerensen, *et al.*, Multi-decadal decline of mercury in the North Atlantic atmosphere explained by changing subsurface seawater concentrations. *Geophys. Res. Lett.* **39** (2012).
23. H. Angot, *et al.*, Global and Local Impacts of Delayed Mercury Mitigation Efforts. *Environ. Sci. Technol.* **52**, 12968–12977 (2018).
24. S. N. Lyman, L. E. Gratz, S. M. Dunham-Cheatham, M. S. Gustin, A. Luippold, Improvements to the Accuracy of Atmospheric Oxidized Mercury Measurements. *Environ. Sci. Technol.* **54**, 13379–13388 (2020).
25. A. Giang, *et al.*, Understanding factors influencing the detection of mercury policies in modelled Laurentian Great Lakes wet deposition. *Environ. Sci.: Processes Impacts* **20**, 1373–1389 (2018).

652 26. M. Iturbide, *et al.*, An update of IPCC climate reference regions for subcontinental analysis of
653      climate model data: definition and aggregated datasets. *Earth Syst. Sci. Data* **12**, 2959–2970
654      (2020).
655 27. Y. Tang, *et al.*, Recent decrease trend of atmospheric mercury concentrations in East China: the
656      influence of anthropogenic emissions. *Atmos. Chem. Phys.* **18**, 8279–8291 (2018).
657 28. P. Sun, *et al.*, Declines of gaseous element mercury concentrations at an urban site in eastern
658      China caused by reductions of anthropogenic emission. *Atmospheric Environment* **317**, 120199
659      (2024).
660 29. M. Muntean, *et al.*, EDGAR v8.1 Global Mercury Emissions. European Commission, Joint Research
661      Centre (JRC) [Dataset] PID: http://data.europa.eu/89h/83b507d7-5218-4dc5-95f9-0ec36f073204.
662      Deposited 2024.
663 30. H. Selin, N. E. Selin, From Stockholm to Minamata and beyond: Governing mercury pollution for a
664      more sustainable future. *One Earth* **5**, 1109–1125 (2022).
665 31. D. G. Streets, *et al.*, Five hundred years of anthropogenic mercury: spatial and temporal release
666      profiles. *Environ. Res. Lett.* **14**, 084004 (2019).
667 32. D. S. Stevenson, *et al.*, Trends in global tropospheric hydroxyl radical and methane lifetime since
668      1850 from AerChemMIP. *Atmos. Chem. Phys.* **20**, 12905–12920 (2020).
669 33. T. S. Dibble, H. L. Tetu, Y. Jiao, C. P. Thackray, D. J. Jacob, Modeling the OH-Initiated Oxidation of
670      Mercury in the Global Atmosphere without Violating Physical Laws. *J. Phys. Chem. A* **124**, 444–453
671      (2020).
672 34. J. P. Parrella, *et al.*, Tropospheric bromine chemistry: implications for present and pre-industrial
673      ozone and mercury. *Atmos. Chem. Phys.* **12**, 6723–6740 (2012).
674 35. A. Saiz-Lopez, *et al.*, Photochemistry of oxidized Hg(I) and Hg(II) species suggests missing mercury
675      oxidation in the troposphere. *Proc. Natl. Acad. Sci. U.S.A.* **117**, 30949–30956 (2020).
676 36. X. Fu, *et al.*, Anthropogenic short-lived halogens increase human exposure to mercury
677      contamination due to enhanced mercury oxidation over continents. *Proc. Natl. Acad. Sci. U.S.A.*
678      **121**, e2315058121 (2024).
679 37. A. Cole, *et al.*, A Survey of Mercury in Air and Precipitation across Canada: Patterns and Trends.
680      *Atmosphere* **5**, 635–668 (2014).
681 38. K. Schaefer, *et al.*, Potential impacts of mercury released from thawing permafrost. *Nat Commun*
682      **11**, 4650 (2020).
683 39. Y. Wang, P. Wu, Y. Zhang, Climate-driven changes of global marine mercury cycles in 2100. *Proc.*
684      *Natl. Acad. Sci. U.S.A.* **120**, e2202488120 (2023).
685 40. B. P. DiMento, R. P. Mason, S. Brooks, C. Moore, The impact of sea ice on the air-sea exchange of
686      mercury in the Arctic Ocean. *Deep Sea Research Part I: Oceanographic Research Papers* **144**, 28–
687      38 (2019).
688 41. A. Kumar, S. Wu, Y. Huang, H. Liao, J. O. Kaplan, Mercury from wildfires: Global emission
689      inventories and sensitivity to 2000–2050 global change. *Atmospheric Environment* **173**, 6–15
690      (2018).
691 42. R. Gelaro, *et al.*, The Modern-Era Retrospective Analysis for Research and Applications, Version 2
692      (MERRA-2). *J. Clim.* **30**, 5419–5454 (2017).
693 43. H. M. Horowitz, *et al.*, A new mechanism for atmospheric mercury redox chemistry: implications for
694      the global mercury budget. *Atmos. Chem. Phys.* **17**, 6353–6371 (2017).
695 44. N. E. Selin, *et al.*, Chemical cycling and deposition of atmospheric mercury: Global constraints from
696      observations. *J. Geophys. Res.* **112**, D02308 (2007).
697 45. Y. Zhang, *et al.*, Improved Anthropogenic Mercury Emission Inventories for China from 1980 to
698      2020: Toward More Accurate Effectiveness Evaluation for the Minamata Convention. *Environ. Sci.*
699      *Technol.* **57**, 8660–8670 (2023).
700 46. Å. Iverfeldt, J. Munthe, C. Brosset, J. Pacyna, "Long-Term Changes in Concentration and
701      Deposition of Atmospheric Mercury Over Scandinavia" in *Mercury as a Global Pollutant:*
702      *Proceedings of the Third International Conference Held in Whistler, British Columbia, July 10–14,*
703      *1994*, D. B. Porcella, J. W. Huckabee, B. Wheatley, Eds. (Springer Netherlands, 1995), pp. 227–
704      233.
705 47. F. Slemr, H. E. Scheel, Trends in atmospheric mercury concentrations at the summit of the Wank
706      mountain, southern Germany. *Atmospheric Environment* **32**, 845–853 (1998).

707  48.  K. Liu, *et al.*, Measure-Specific Effectiveness of Air Pollution Control on China's Atmospheric
708      Mercury Concentration and Deposition during 2013–2017. *Environ. Sci. Technol.* **53**, 8938–8946
709      (2019).
710  49.  Q. Wu, *et al.*, Temporal Trend and Spatial Distribution of Speciated Atmospheric Mercury Emissions
711      in China During 1978–2014. *Environ. Sci. Technol.* **50**, 13428–13435 (2016).
712  50.  M. Muntean, *et al.*, Trend analysis from 1970 to 2008 and model evaluation of EDGARv4 global
713      gridded anthropogenic mercury emissions. *Science of The Total Environment* **494–495**, 337–350
714      (2014).
715  51.  H. M. Horowitz, D. J. Jacob, H. M. Amos, D. G. Streets, E. M. Sunderland, Historical Mercury
716      Releases from Commercial Products: Global Environmental Implications. *Environ. Sci. Technol.* **48**,
717      10242–10250 (2014).
718  52.  S. Y. Kwon, *et al.*, Mercury stable isotopes for monitoring the effectiveness of the Minamata
719      Convention on Mercury. *Earth-Science Reviews* **203**, 103111 (2020).
720  53.  J. A. Fisher, *et al.*, A synthesis of mercury research in the Southern Hemisphere, part 2:
721      Anthropogenic perturbations. *Ambio* **52**, 918–937 (2023).
722  54.  L. Schneider, *et al.*, A synthesis of mercury research in the Southern Hemisphere, part 1: Natural
723      processes. *Ambio* **52**, 897–917 (2023).
724  55.  D. S. McLagan, *et al.*, A High-Precision Passive Air Sampler for Gaseous Mercury. *Environ. Sci.
725      Technol. Lett.* **3**, 24–29 (2016).
726  56.  S. M. Dunham-Cheatham, S. Lyman, M. S. Gustin, Comparison and calibration of methods for
727      ambient reactive mercury quantification. *Science of The Total Environment* **856**, 159219 (2023).
728  57.  A. Luippold, *et al.*, Use of Multiple Lines of Evidence to Understand Reactive Mercury
729      Concentrations and Chemistry in Hawai'i, Nevada, Maryland, and Utah, USA. *Environ. Sci. Technol.*
730      **54**, 7922–7931 (2020).
731  58.  F. De Simone, *et al.*, A Chemical Transport Model Emulator for the Interactive Evaluation of Mercury
732      Emission Reduction Scenarios. *Atmosphere* **11**, 878 (2020).
733  59.  C. W. Tessum, J. D. Hill, J. D. Marshall, InMAP: A model for air pollution interventions. *PLoS ONE*
734      **12**, e0176131 (2017).
735  60.  W. Atkinson, *et al.*, A tool for air pollution scenarios (TAPS v1.0) to enable global, long-term, and
736      flexible study of climate and air quality policies. *Geosci. Model Dev.* **15**, 7767–7789 (2022).
737  61.  A. Dastoor, *et al.*, The Multi-Compartment Hg Modeling and Analysis Project (MCHgMAP): Mercury
738      modeling to support international environmental policy. *Geoscientific Model Development
739      Discussions* **2024**, 1–171 (2024).
740  62.  P. J. Blanchfield, *et al.*, Experimental evidence for recovery of mercury-contaminated fish
741      populations. *Nature* **601**, 74–78 (2022).
742  63.  A. Steffen, *et al.*, A synthesis of atmospheric mercury depletion event chemistry in the atmosphere
743      and snow. *Atmospheric Chemistry and Physics* **8**, 1445–1482 (2008).
744  64.  M. S. Gustin, *et al.*, Do We Understand What the Mercury Speciation Instruments Are Actually
745      Measuring? Results of RAMIX. *Environ. Sci. Technol.* **47**, 7295–7306 (2013).
746  65.  D. A. Gay, *et al.*, The Atmospheric Mercury Network: measurement and initial examination of an
747      ongoing atmospheric mercury record across North America. *Atmos. Chem. Phys.* **13**, 11339–11349
748      (2013).
749  66.  K. Tørseth, *et al.*, Introduction to the European Monitoring and Evaluation Programme (EMEP) and
750      observed atmospheric composition change during 1972–2009. *Atmos. Chem. Phys.* **12**, 5447–5481
751      (2012).
752  67.  F. Sprovieri, *et al.*, Atmospheric mercury concentrations observed at ground-based monitoring sites
753      globally distributed in the framework of the GMOS network. *Atmos. Chem. Phys.* **16**, 11915–11935
754      (2016).
755  68.  V. L. St. Louis, *et al.*, Atmospheric Concentrations and Wet/Dry Loadings of Mercury at the Remote
756      Experimental Lakes Area, Northwestern Ontario, Canada. *Environ. Sci. Technol.* **53**, 8017–8026
757      (2019).
758  69.  F. Carbone, *et al.*, Sea surface temperature variation linked to elemental mercury concentrations
759      measured on Mauna Loa. *Geophys. Res. Lett.* **43**, 7751–7757 (2016).
760  70.  M. S. Landis, R. K. Stevens, F. Schaedlich, E. M. Prestbo, Development and Characterization of an
761      Annular Denuder Methodology for the Measurement of Divalent Inorganic Reactive Gaseous
762      Mercury in Ambient Air. *Environ. Sci. Technol.* **36**, 3000–3009 (2002).

763 71. S. Sholupov, S. Pogarev, V. Ryzhov, N. Mashyanov, A. Stroganov, Zeeman atomic absorption
764      spectrometer RA-915+ for direct determination of mercury in air and complex matrix samples. *Fuel*
765      *Processing Technology* **85**, 473–485 (2004).
766 72. Å. Iverfeldt, Occurrence and turnover of atmospheric mercury over the nordic countries. *Water, Air,*
767      *and Soil Pollution* **56**, 251–265 (1991).
768 73. K.-L. Chang, M. G. Schultz, G. Koren, Selke, Niklas, Guidance note on best statistical practices for
769      TOAR analyses. Available at: https://doi.org/10.48550/arXiv.2304.14236. (2023).
770 74. D. Bates, M. Mächler, B. Bolker, S. Walker, Fitting Linear Mixed-Effects Models Using **lme4**. *J. Stat.*
771      *Soft.* **67** (2015).
772 75. R. Koenker, K. F. Hallock, Quantile Regression. *The Journal of Economic Perspectives* **15**, 143–
773      156 (2001).
774 76. K.-L. Chang, *et al.*, Impact of the COVID-19 Economic Downturn on Tropospheric Ozone Trends:
775      An Uncertainty Weighted Data Synthesis for Quantifying Regional Anomalies Above Western North
776      America and Europe. *AGU Advances* **3**, e2021AV000542 (2022).
777 77. W. C. Porter, C. L. Heald, D. Cooley, B. Russell, Investigating the observed sensitivities of air-
778      quality extremes to meteorological drivers via quantile regression. *Atmos. Chem. Phys.* **15**, 10349–
779      10366 (2015).
780 78. R. Koenker, quantreg: Quantile Regression. Available at: https://CRAN.R-
781      project.org/package=quantreg. (2022).
782 79. A. Feinberg, T. Dlamini, M. Jiskra, V. Shah, N. E. Selin, Evaluating atmospheric mercury (Hg)
783      uptake by vegetation in a chemistry-transport model. *Environ. Sci.: Processes Impacts* **24**, 1303–
784      1318 (2022).
785 80. M. D. McKay, R. J. Beckman, W. J. Conover, Comparison of Three Methods for Selecting Values of
786      Input Variables in the Analysis of Output from a Computer Code. *Technometrics* **21**, 239–245
787      (1979).
788 81. N. E. Selin, A proposed global metric to aid mercury pollution policy. *Science* **360**, 607–609 (2018).
789 82. H. M. Amos, *et al.*, Global Biogeochemical Implications of Mercury Discharges from Rivers and
790      Sediment Burial. *Environ. Sci. Technol.* **48**, 9514–9522 (2014).
791 83. P. D. Nightingale, *et al.*, In situ evaluation of air-sea gas exchange parameterizations using novel
792      conservative and volatile tracers. *Global Biogeochem. Cycles* **14**, 373–387 (2000).
793 84. S. Song, *et al.*, Top-down constraints on atmospheric mercury emissions and implications for global
794      biogeochemical cycling. *Atmos. Chem. Phys.* **15**, 7103–7125 (2015).
795 85. N. E. Selin, *et al.*, Global 3-D land-ocean-atmosphere model for mercury: Present-day versus
796      preindustrial cycles and anthropogenic enrichment factors for deposition. *Global Biogeochem.*
797      *Cycles* **22**, GB2011 (2008).
798 86. G. R. van der Werf, *et al.*, Global fire emissions estimates during 1997–2016. *Earth Syst. Sci. Data*
799      **9**, 697–720 (2017).

800
801

802 **Figures**



803
804 **Figure 1.** Map of observation stations that measured atmospheric Hg concentrations for more than 6
805 years (Table S1). Defined regions (26) are indicated with black lines, with corresponding numbering of
806 included regions listed on the map. For this study, we included NH stations with openly accessible or
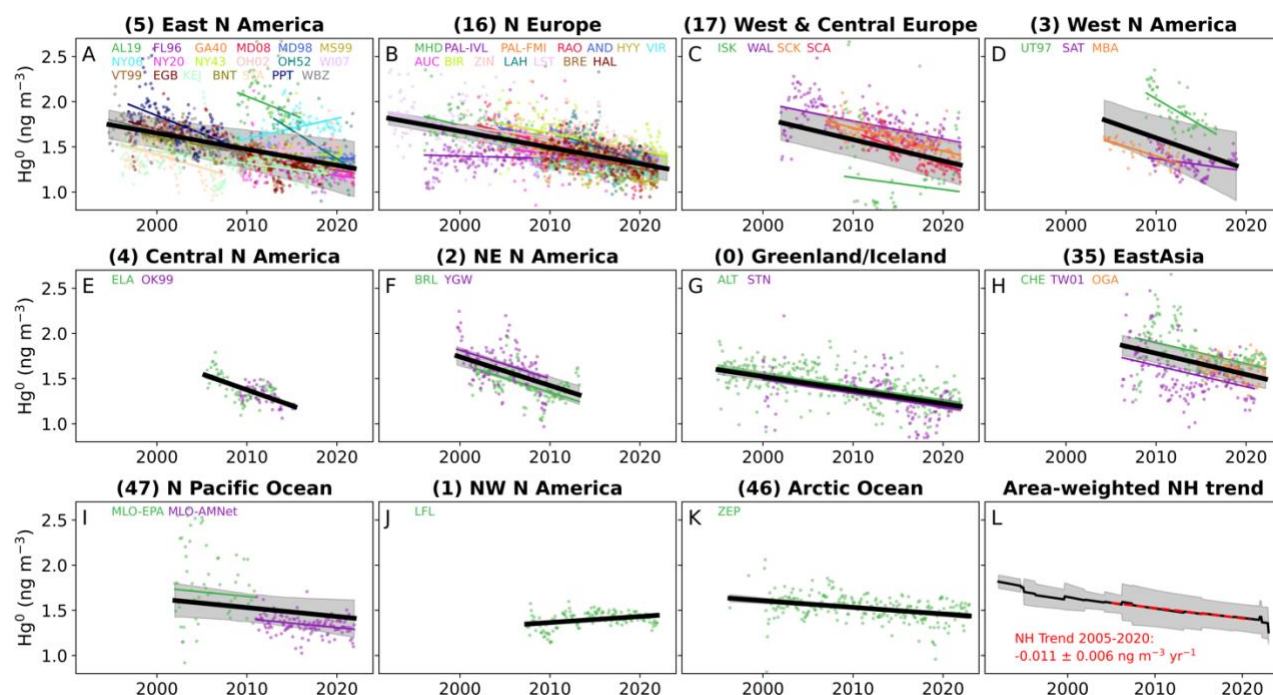807 provided datasets.
808

809
810 **Figure 2.** Trends in observed gaseous elemental mercury (Hg$^0$) aggregated by the regions (*A–K*) in Fig. 1
811 (labelled by region number). Trends are calculated with linear mixed effects modeling, with overall
812 regional trends shown in black and shading shows the 5$^{th}$ to 95$^{th}$ percentile range. Individual site
813 deseasonalized monthly means are shown as colored points and individual regressions as colored lines.
814 The overall Northern Hemisphere (NH) trend (*L*) is calculated by taking the area-weighted average of
815 regional trends, with the shading showing the 2σ averaging error. The red dashed curve in *L* is the linear
816 regression trend for 2005–2020, with trend error representing 2σ error from resampling regional trends
817 within their error bounds. We distinguished data from sites where measurements were made by multiple
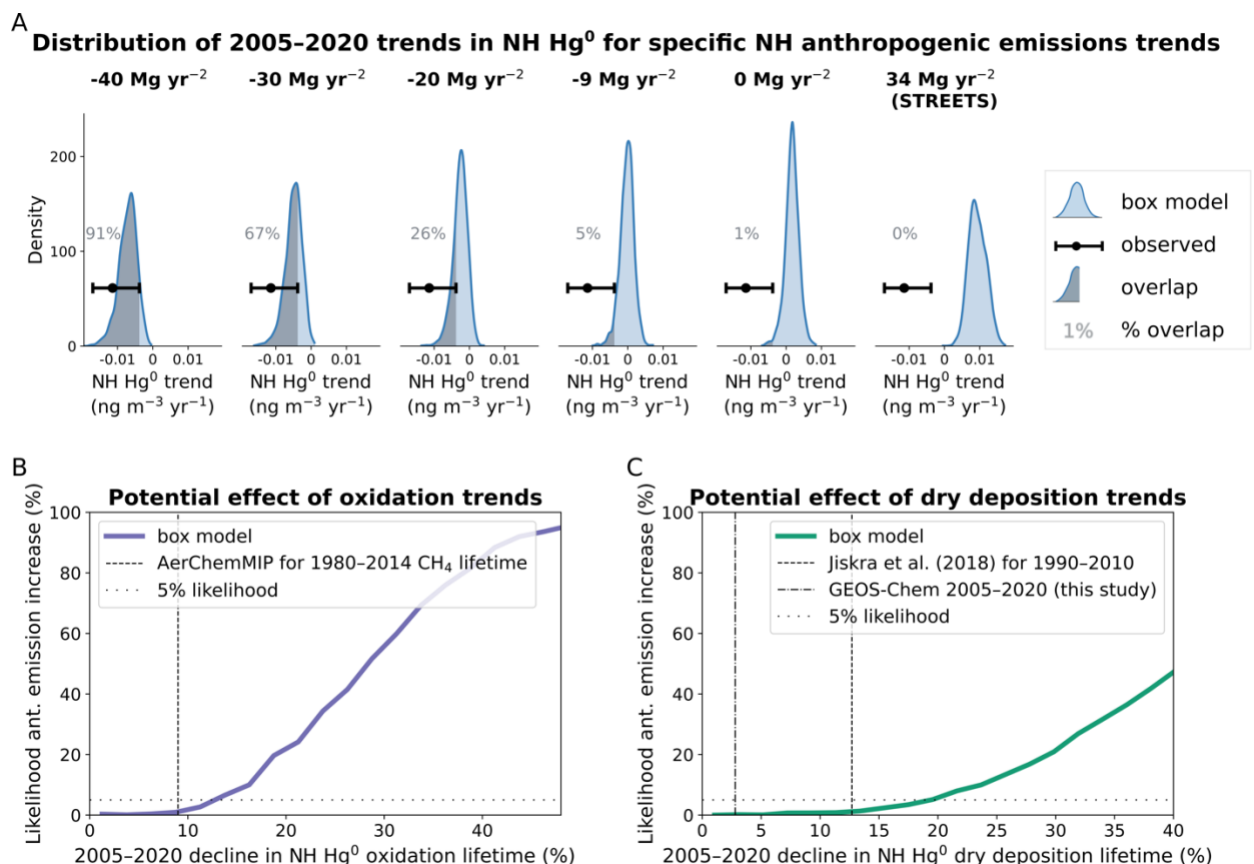818 networks, i.e., Pallas (FMI and IVL) and Mauna Loa (EPA and AMNet).
819
820

**Figure 3.** Modeled relationships between 2005–2020 trends in NH Hg$^0$ concentrations and drivers. (*A*) Histograms showing relationship between 2005–2020 trends in anthropogenic NH emissions and NH Hg$^0$ trends. We select scenarios with different anthropogenic emissions trend values from the $10^5$ box model simulations (with a window of ±1 Mg yr$^{-2}$ to yield ~2000 simulations for each trend value). Blue histograms illustrate the probability density of simulated NH Hg$^0$ trends for each emission trend value. Observed NH Hg$^0$ trends are shown in the horizontal black line with error bars. The shaded overlap represents the area of the histogram where the model is compatible with observed trends, with the percent of total area shown in grey. The histogram for the anthropogenic emissions trend of 34 Mg yr$^{-2}$ represents the Streets et al. (10) 2005–2015 trend. (*B*) Impact of NH Hg$^0$ oxidation lifetime trends on the likelihood of positive anthropogenic (ant.) trends for 2005–2020. The x-axis shows the relative decline (%) in the NH Hg$^0$ oxidation lifetime between 2005 and 2020. The y-axis refers to the percent of box model runs fitting with the observed NH Hg$^0$ trend (± 2σ) that have positive anthropogenic emissions trends. The AerChemMIP (32) estimate for the relative change 1980-2014 methane (CH$_4$) oxidation lifetime is shown for context. (*C*) Impact of NH Hg$^0$ dry deposition lifetime on the likelihood of positive anthropogenic (ant.) trends for 2005–2020. The x-axis shows the relative decline (%) in the NH Hg$^0$ dry deposition lifetime between 2005 and 2020. The estimated trend in NH dry deposition from Jiskra et al. (20) for 1990–2010 is shown for context, as well as the GEOS-Chem simulated 2005–2020 trend (Fig. S11).
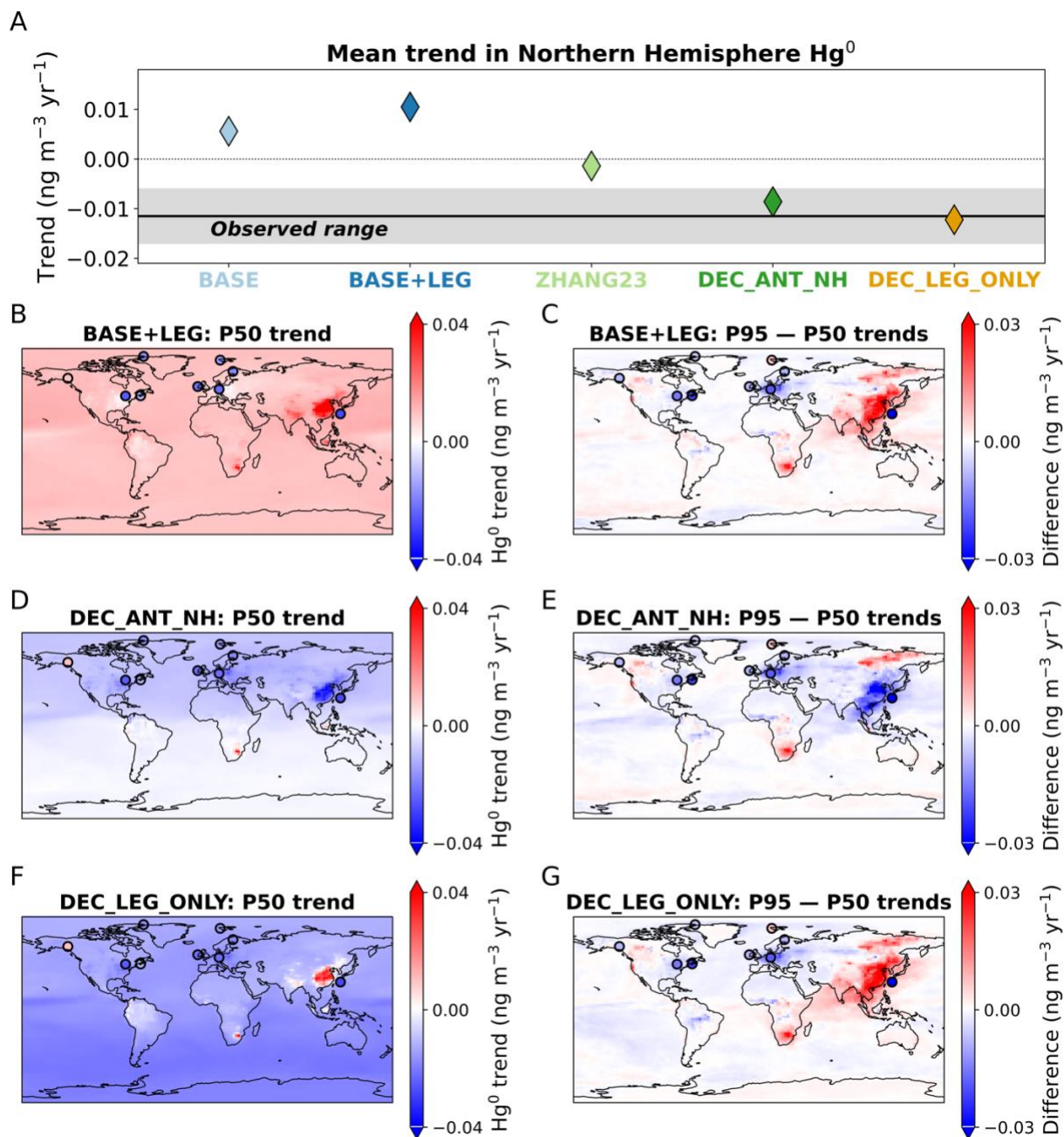
840
841 **Figure 4.** Comparison between trends (2005–2020) in GEOS-Chem model simulations and observations
842 for Northern Hemisphere (NH) mean $Hg^0$ (*A*), calculated using linear mixed effects modeling of available
843 NH regions and calculating the area-weighted mean (Fig. 2). The observed range in the NH $Hg^0$ trend is
844 shown as a black line (mean) with shaded area (±2σ). Error bars are smaller than the markers for the
845 model simulations. Trend in median (P50) daily deseasonalized simulated values in BASE+LEG (*B*),
846 DEC_ANT_NH (*D*), and DEC_LEG_ONLY (*F*) for each model grid cell. BASE+LEG is the simulation with
847 Streets et al. (10) emissions and associated legacy feedbacks, DEC_ANT_NH is the simulation with
848 decreasing anthropogenic emissions in the NH, and DEC_LEG_ONLY includes a decline in legacy
849 emissions from the ocean (Table 1). Observed results are plotted in filled circles for 9 stations with more
850 than 13 years of high frequency data. Differences between 95th percentile (P95) trend and median (P50)
851 trend shown for BASE+LEG (*C*), DEC_ANT_NH (*E*), and DEC_LEG_ONLY (*G*) simulations and
852 observations. The other simulations are shown in Fig. S13.

853    **Table 1**. Description of Hg simulations conducted in GEOS-Chem for 2005–2020.

| Simulation | Anthropogenic emissions | Legacy re-emissions | Anthropogenic NH emissions trend (Mg yr$^{-2}$) | Overall NH emissions trend (Mg yr$^{-2}$) |
|---|---|---|---|---|
| BASE | 2005–2015: Streets et al. (10) 2016–2020: repeat 2015 | Constant interannually; based on Horowitz et al. (43) | +23 | +18 |
| BASE+LEG | 2005–2015: Streets et al. (10) 2016–2020: repeat 2015 | Trend from median response to BASE anthropogenic emissions trend (Fig. S9F) | +23 | +31 |
| ZHANG23 | 2005–2020 Chinese emissions from BASE are scaled by emission inventory trend from Zhang et al. (45) | Trend from median response to ZHANG23 anthropogenic emissions trend (Fig. S9F) | −11 | −12 |
| DEC_ANT_NH | ZHANG23 emissions with additional 23 Mg yr$^{-2}$ decrease in anthropogenic emissions spread across NH outside China | Trend from median response to DEC_ANT_NH anthropogenic emissions trend (Fig. S9F) | −34 | −41 |
| DEC_LEG_ONLY | 2005–2015: Streets et al. (10) 2016–2020: repeat 2015 | Decline imposed | +23 | −30 |

854

1    **Supplementary Information (SI) for**

2    Unexpected anthropogenic emission decreases explain recent atmospheric mercury

3    concentration declines

4

5    Aryeh Feinberg[a]*, Noelle E. Selin[a,b], Christine F. Braban[c], Kai-Lan Chang[d,e], Danilo Custódio[f], Daniel A.

6    Jaffe[g,h], Katriina Kyllönen[i], Matthew S. Landis[j], Sarah R. Leeson[c], Winston Luke[k], Koketso M. Molepo[l],

7    Marijana Murovec[m], Michelle G. Nerentorp Mastromonaco[n], Katrine Aspmo Pfaffhuber[o], Julian Rüdiger[p],

8    Guey-Rong Sheu[q], and Vincent L. St.Louis[r]

9    [a] *Institute for Data, Systems, and Society, Massachusetts Institute of Technology, Cambridge, MA 02139,*

10   *USA*

11   [b] *Department of Earth, Atmospheric, and Planetary Sciences, Massachusetts Institute of Technology,*

12   *Cambridge, MA 02139, USA*

13   [c] *UK Centre for Ecology & Hydrology (UKCEH), Penicuik, Midlothian EH26 0QB, UK*

14   [d] *Cooperative Institute for Research in Environmental Sciences, University of Colorado, Boulder, CO*

15   *80309-0401, USA*

16   [e] *NOAA Chemical Sciences Laboratory, Boulder, CO 80305, USA*

17   [f] *Max-Planck-Institut für Biogeochemie, D-07745 Jena, Germany*

18   [g] *School of STEM, University of Washington Bothell, Bothell, WA 98011, USA*

19   [h] *Department of Atmospheric Sciences, University of Washington Seattle, Seattle, WA 98195, USA*

20   [i] *Finnish Meteorological Institute, Helsinki 00560, Finland*

21   [j] *United States Environmental Protection Agency, Office of Research and Development, Research*

22   *Triangle Park, NC 27711, USA*

23   [k] *NOAA/Air Resources Laboratory, College Park, MD 20740, USA*

24   [l] *Institute of Coastal Environmental Chemistry, Helmholtz Zentrum Hereon, 21502 Geesthacht, Germany*

25   [m] *Slovenian Environment Agency, Environment and Nature protection Office, Air Quality Division,1000*

26   *Ljubljana, Slovenia*

27   [n] *IVL Swedish Environmental Research Institute, SE-411 33 Gothenburg, Sweden*

28   [o] *NILU, 2027 Kjeller, Norway*

29   [p] *Air Monitoring Network, German Environment Agency, 63225 Langen, Germany*

30   [q] *Department of Atmospheric Sciences, National Central University, Taoyuan 320, Taiwan*

31   [r] *Department of Biological Sciences, University of Alberta, Edmonton, AB T6G 2E9, Canada*

32   *Correspondence to: arifeinberg@gmail.com (A.F.)

33   **This PDF file includes:**

34          Supplementary Text
35          Figures S1 to S15
36          Tables S1 to S4
37          Supplementary References

**Section S1. Observation station information**

**Table S1**. List of sites measuring gaseous elemental mercury (GEM: $Hg^0$) or total gaseous mercury (TGM) included in this study.

| Site code | Location | Latitude | Longitude | Measurement network | IPCC region[a] | Years available | Measured quantity |
|---|---|---|---|---|---|---|---|
| AL19 | Birmingham, USA | 33.6 | -86.8 | AMNet[b] | 5 | 2009–2015 | $Hg^0$ |
| FL96 | Pensacola, USA | 30.5 | -87.4 | AMNet[b] | 5 | 2009–2015 | $Hg^0$ |
| GA40 | Yorkville, USA | 33.9 | -85.0 | AMNet[b] | 5 | 2009–2015 | $Hg^0$ |
| MD08 | Piney Reservoir, USA | 39.7 | -79.0 | AMNet[b] | 5 | 2009–2021 | $Hg^0$ |
| MD98 | Beltsville, USA | 39.0 | -76.8 | AMNet[b] | 5 | 2009–2021 | $Hg^0$ |
| MS99 | Grand Bay, USA | 30.4 | -88.4 | AMNet[b] | 5 | 2009–2020 | $Hg^0$ |
| NY06 | Bronx, USA | 40.9 | -73.9 | AMNet[b] | 5 | 2008–2020 | $Hg^0$ |
| NY20 | Huntington Forest, USA | 44.0 | -74.2 | AMNet[b] | 5 | 2009–2021 | $Hg^0$ |
| NY43 | Rochester, USA | 43.1 | -77.5 | AMNet[b] | 5 | 2008–2020 | $Hg^0$ |
| OH02 | Athens, USA | 39.3 | -82.1 | AMNet[b] | 5 | 2009–2020 | $Hg^0$ |
| OH52 | South Bass Island, USA | 41.7 | -82.8 | AMNet[b] | 5 | 2013–2021 | $Hg^0$ |
| OK99 | Stilwell, USA | 35.8 | -94.7 | AMNet[b] | 4 | 2009–2015 | $Hg^0$ |
| UT97 | Salt Lake City, USA | 40.7 | -112.0 | AMNet[b] | 3 | 2008–2017 | $Hg^0$ |
| VT99 | Underhill, USA | 44.5 | -72.9 | AMNet[b] | 5 | 2009–2016 | $Hg^0$ |
| WI07 | Horicon Marsh, USA | 43.5 | -88.6 | AMNet[b] | 5 | 2011–2017 | $Hg^0$ |
| MLO | Mauna Loa, USA | 19.5 | -155.6 | AMNet[b]/EPA[c]/NOAA | 47 | 2002–2021 | $Hg^0$ |
| MBA | Mt. Bachelor, USA | 44.0 | -121.7 | GMOS[d] | 3 | 2004–2012 | $Hg^0$ / TGM[*] |
| ALT | Alert, Canada | 82.5 | -62.3 | ECCC[e] | 0 | 1995–2021 | $Hg^0$ / TGM[†] |
| BNT | Burnt Island, Canada | 45.8 | -82.9 | ECCC[e] | 5 | 1998–2007 | TGM |
| BRL | Bratt's Lake, Canada | 50.2 | -104.7 | ECCC[e] | 2 | 2001–2013 | TGM |
| EGB | Egbert, Canada | 44.2 | -79.8 | ECCC[e] | 5 | 1996–2018 | TGM |
| KEJ | Kejimkujik, Canada | 44.4 | -65.2 | AMNet[b]/ ECCC[e] | 5 | 1996–2018 | $Hg^0$ / TGM[‡] |
| LFL | Little Fox Lake, Canada | 61.4 | -135.6 | ECCC[e] | 1 | 2007–2021 | TGM |
| PPT | Point Petre, Canada | 43.8 | -77.1 | ECCC[e] | 5 | 1996–2007 | TGM |
| SAT | Saturna, Canada | 48.8 | -123.2 | ECCC[e] | 3 | 2009–2018 | TGM |
| STA | Huntsman Science Centre, Canada | 45.1 | -67.1 | ECCC[e] | 5 | 1995–2007 | TGM |
| WBZ | St. Anicet, Canada | 45.1 | -74.3 | ECCC[e] | 5 | 1994–2009 | TGM |
| YGW | Kuujuarapik, Canada | 55.3 | -77.7 | ECCC[e] | 2 | 1999–2009 | TGM |
| ELA | Experimental Lakes Area, Canada | 49.7 | -93.7 | IISD[f] | 4 | 2005–2013 | $Hg^0$ |
| AND | Andøya, Norway | 69.3 | 16.0 | EMEP[g] | 16 | 2004–2021 | $Hg^0$ |
| AUC | Auchencorth Moss, UK | 55.8 | -3.2 | EMEP[g] | 16 | 2006–2022 | $Hg^0$ / TGM[#] |
| BIR | Birkenes, Norway | 58.4 | 8.3 | EMEP[g] | 16 | 2004–2023 | $Hg^0$ / TGM[§] |
| BRE | Bredkälen, Sweden | 63.9 | 15.3 | EMEP[g] | 16 | 2009–2021 | TGM |
| HAL | Hallahus/Vavihill[h], Sweden | 56.0 | 13.1 | EMEP[g] | 16 | 2009–2021 | TGM |
| HYY | Hyytiälä, Finland | 61.6 | 24.0 | EMEP[g] | 16 | 2009–2021 | TGM |
| ISK | Iskrba, Slovenia | 45.6 | 14.9 | EMEP[g] | 17 | 2009–2021 | TGM |
| LAH | Lahemaa, Estonia | 59.5 | 25.9 | EMEP[g] | 16 | 2012–2021 | $Hg^0$ |
| LST | Lista, Norway | 58.1 | 6.6 | EMEP[g] | 16 | 1992–2004 | TGM |
| MHD | Mace Head, Ireland | 53.3 | -9.9 | EMEP[g]/GMOS[d] | 16 | 1996–2022 | TGM |
| PAL | Pallas, Finland | 68.0 | 24.4 | EMEP[g]/GMOS[d] | 16 | 1996–2021 | TGM |
| RAO | Råö, Sweden | 57.4 | 11.9 | EMEP[g]/GMOS[d] | 16 | 2002–2020 | TGM |
| SCA | Schauinsland, Germany | 47.9 | 7.9 | EMEP[g] | 17 | 2011–2021 | TGM |
| SCK | Schmücke, Germany | 50.7 | 10.8 | EMEP[g] | 17 | 2007–2021 | TGM |
| STN | Station Nord/Villum, Greenland | 81.6 | -16.6 | EMEP[g] | 0 | 2000–2021 | TGM |
| VIR | Virolahti, Finland | 60.5 | 27.7 | EMEP[g] | 16 | 2008–2021 | TGM |
| WAL | Waldhof, Germany | 52.8 | 10.8 | EMEP[g] | 17 | 2002–2021 | TGM |
| ZEP | Zeppelin, Norway | 78.9 | 11.9 | EMEP[g] | 46 | 1996–2022 | $Hg^0$ / TGM[¶] |
| ZIN | Zingst, Germany | 54.4 | 12.7 | EMEP[g] | 16 | 1999–2021 | TGM |
| TW01 | Mt. Lulin, Taiwan | 23.5 | 120.9 | AMNet[b] / MOENV Taiwan[i] | 35 | 2006–2020 | $Hg^0$ |
| CHE | Cape Hedo, Japan | 26.9 | 128.3 | MOEJ[j] | 35 | 2007–2022 | $Hg^0$ |
| OGA | Oga Peninsula, Japan | 39.9 | 139.9 | MOEJ[j] | 35 | 2014–2022 | $Hg^0$ |

[a] IPCC regions are defined with the numbering in Fig. 1, taken from Iturbide et al. (1)   [b] Gay et al. (2)   [c] Carbone et al. (3)
[d] Sprovieri et al. (4)   [e] Cole et al. (5)   [f] St. Louis et al. (6)   [g] Tørseth et al. (7)   [h] Site changed location in 2016, but due to nearby locations (<3 km apart), they are combined in this analysis   [i] Nguyen et al. (8)   [j] Marumoto et al. (9)
[*] MBA: TGM (2004) and $Hg^0$ (2005–2012)   [†] ALT: TGM (1995–2021) and $Hg^0$ (2002–2021); analyzed TGM
[‡] KEJ: TGM (1996–2018) and $Hg^0$ (2009–2018); analyzed TGM   [#] AUC: TGM (2006–2013) and $Hg^0$ (2012–2022)
[§] BIR: TGM (2004–2010) and $Hg^0$ (2011–2023)   [¶] ZEP: TGM (1996–2000) and $Hg^0$ (2000–2022)
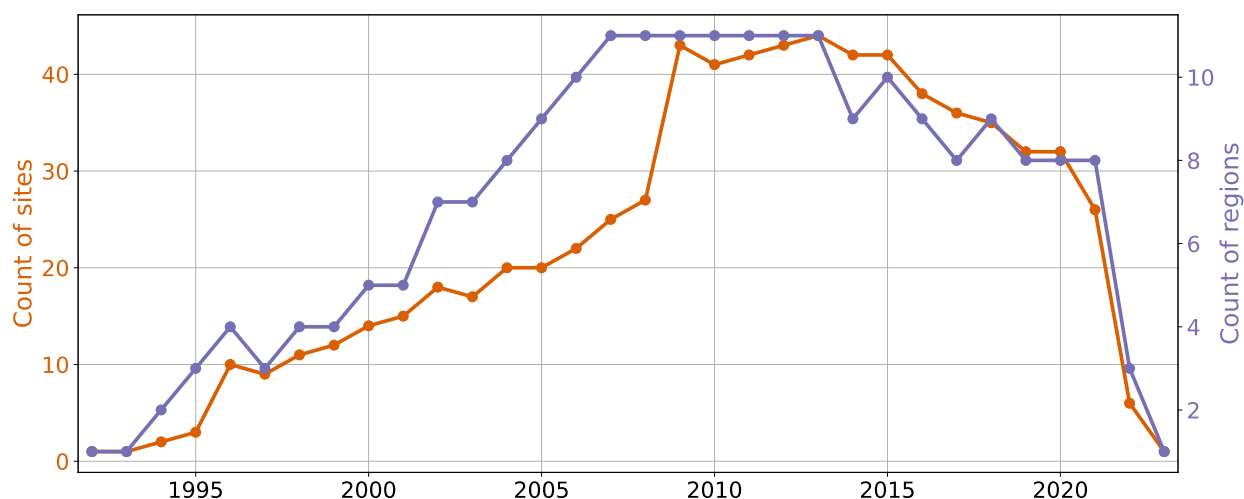
47
48  **Figure S1.** Timeseries showing count of measurement sites included in this study by operation year. The
49  orange curve shows the number of sites measured in each year and the purple curve shows the number
50  of Northern Hemisphere (NH) IPCC regions (Fig. 1) measured in each year. Note that 2022 and 2023
51  data may still be undergoing quality control procedures by networks and therefore was not yet released at
52  the time of analysis; more data from these years will likely be made available in the future.

53
54  **Section S2. Trend results by region**

55
56  **Table S2**. Tabulated overall regional trends (± 2σ) calculated through linear mixed effects modelling for
57  full available time period of each region.

| Region name (number) | Number of sites | Area (10⁶ km²) | Trend (ng m⁻³ yr⁻¹) | Time period |
|---|---|---|---|---|
| Eastern North America (5) | 19 | 5.69 | -0.016 ± 0.011 | 1994–2022 |
| Northern Europe (16) | 13 | 5.00 | -0.018 ± 0.004 | 1992–2023 |
| West & Central Europe (17) | 4 | 3.79 | -0.024 ± 0.010 | 2002–2021 |
| Western North America (3) | 3 | 3.14 | -0.035 ± 0.025 | 2004–2018 |
| Central North America (4) | 2 | 2.93 | -0.035 ± 0.007 | 2005–2015 |
| Northeastern North America (2) | 2 | 7.66 | -0.032 ± 0.009 | 1999–2013 |
| Greenland/Iceland (0) | 2 | 4.77 | -0.015 ± 0.003 | 1995–2021 |
| East Asia (35) | 3 | 9.46 | -0.023 ± 0.005 | 2006–2022 |
| North Pacific Ocean (47) | 1 | 51.61 | -0.010 ± 0.011 | 2002–2021 |
| Northwestern North America (1) | 1 | 7.51 | 0.007 ± 0.003 | 2007–2021 |
| Arctic Ocean (1) | 1 | 6.35 | -0.007 ± 0.002 | 1996–2022 |
| **Northern Hemisphere (NH) area-weighted average** | **51** | | **-0.011 ± 0.006** | **2005–2020** |

58
59

60 **Section S3. Sensitivity of trends to statistical approach**
61 *Section S3.1 Modelled differences between site, surface, and troposphere NH trends*
62 We used the five GEOS-Chem simulations to test different approaches for calculating overall trends in NH
63 $Hg^0$ (Fig. S2). We calculated annual averages of the model results over the entire NH troposphere
64 (orange lines), representative of the NH tropospheric box in the 3-box model simulations. We compared
65 this to simulated NH surface $Hg^0$ concentrations (purple lines), which is the quantity that can actually be
66 measured by surface observation stations. The calculated 2005–2020 trends in surface $Hg^0$ agree within
67 0.0007 ng $m^{-3}$ $yr^{-1}$ of tropospheric $Hg^0$ trends for all simulations except DEC_ANT_NH, where surface
68 declines are faster than tropospheric declines by 0.0015 ng $m^{-3}$ $yr^{-1}$. This can be explained by enhanced
69 dilution of the negative emissions trends when considering the whole troposphere versus the surface
70 level. To approximate the real situation where only a small fraction of the NH surface is measured, we
71 averaged only the model grid cells that contain the 51 observation sites (magenta line in Fig. S2). This
72 approach leads to biases of up to 0.0044 ng $m^{-3}$ $yr^{-1}$ due to the uneven distribution of observation stations
73 (Fig. 1) throughout the NH, with some regions covered more than others and other regions having no
74 observations. This bias can be reduced to below 0.0006 ng $m^{-3}$ $yr^{-1}$ by first averaging by IPCC region the
75 grid cells that correspond to observation sites (Fig. 1) and then calculating an area-weighted average for
76 the NH (green line), similar to what was done for the observation analysis in the main manuscript (Fig. 2).
77 Therefore, it is best to use the approach of area-weighted site averages when limited observation stations
78 are available, leading to good agreement with the surface trends in $Hg^0$. We expanded the observed trend
79 uncertainty in Figs. 3A and B upwards by 0.0021 ng $m^{-3}$ $yr^{-1}$ (max error between area-weighted and
80 tropospheric trends, DEC_ANT_NH), due to the potential overestimate of NH tropospheric trends by only
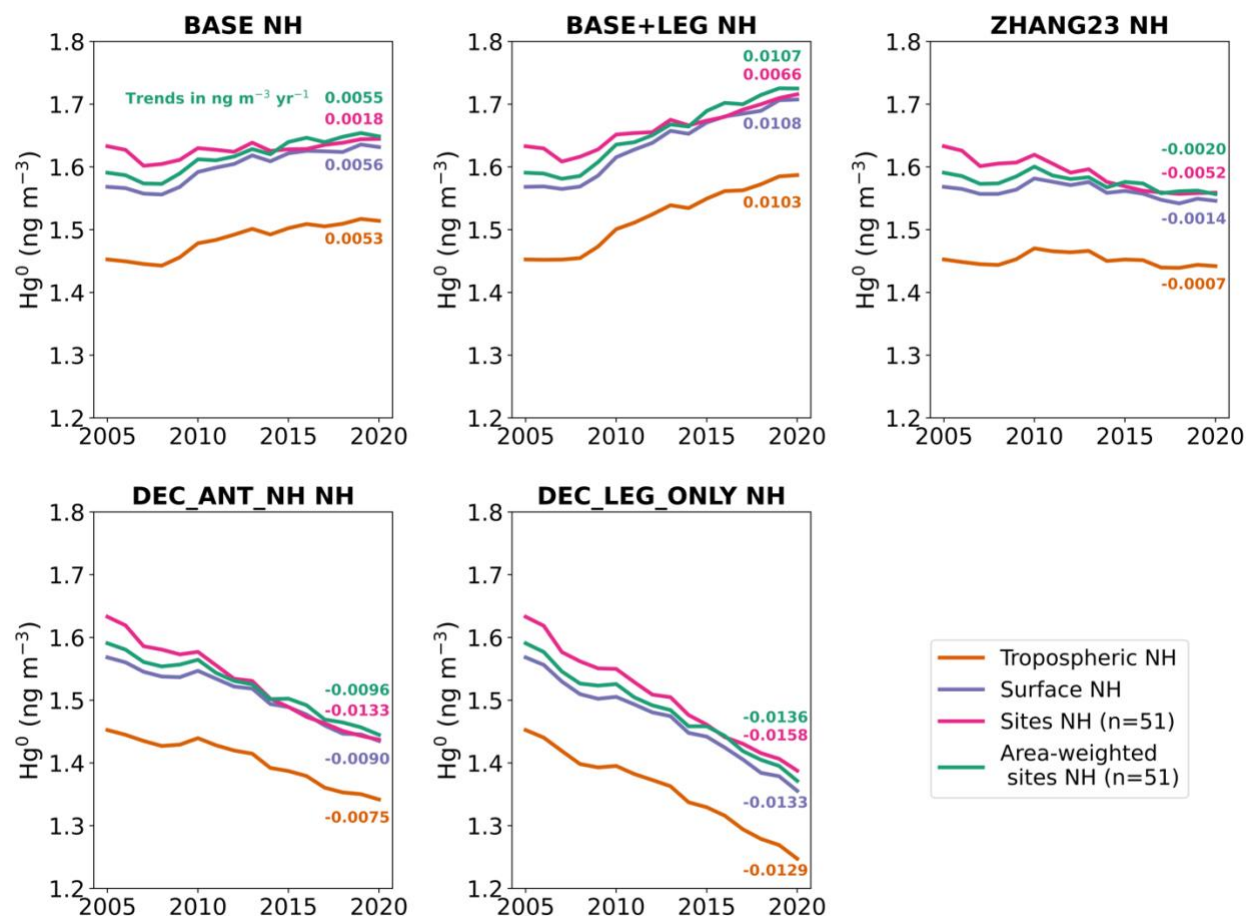81 having surface observations (Fig. S2).
82

**Figure S2.** Different methods of calculating hemispheric average trends applied to GEOS-Chem simulated $Hg^0$. We compared annual mean simulated timeseries of: 1) NH tropospheric averages, 2) NH surface averages, 3) averaging model grid cells where observation sites are located, and 4) area-weighted averaging of regional averages of model grid cells where observation sites are located. Linear regression trends over 2005–2020 are listed in units of ng m$^{-3}$ yr$^{-1}$.

*Section S3.2 Aggregation of observation stations into overall NH annual averages using "bucket" method*
Previous studies (e.g., 10) have calculated overall timeseries for regions by averaging all available stations for each specific year ("bucket" method). Biases can arise in this approach from multiple sources of error: 1) sites have individual offsets and trends due to measurement method differences or specific local sources, leading to biases in a "bucket" average because sites do not all cover the same time period; 2) sites are unevenly distributed, with certain regions over- or under-represented; and 3) certain months can be missing in a specific year, which due to the strong seasonality of $Hg^0$ can bias the annual mean. We aimed to address the drawbacks of the "bucket" approach by explicitly modeling offsets between sites using linear mixed effects models, deseasonalizing monthly means from all observations, and aggregating results by IPCC regions before calculating area-weighted averages. To compare our methods with approaches applied in previous papers, we use the bucket approach to calculate 2005–2020 trends in Eastern North America (19 sites), Northern Europe (13 sites), and the NH (51 sites) (Fig. S3) in a sensitivity test. Overall, the derived trends are similar for the NH between our approach (-0.011 ± 0.006 ng m$^{-3}$ yr$^{-1}$) and the "bucket" approach (-0.015 ng m$^{-3}$ yr$^{-1}$). Issues with the bucket method were observed for periods when less sites are available (e.g., before the year 2000 in Fig. S3), which show high variability due to differences in the number and characteristics of averaged sites for each year.

106 Therefore, we recommend that caution be exercised with such an approach, as the derived aggregated
107 timeseries may be misleading and could be misinterpreted as real variability rather than changes in site
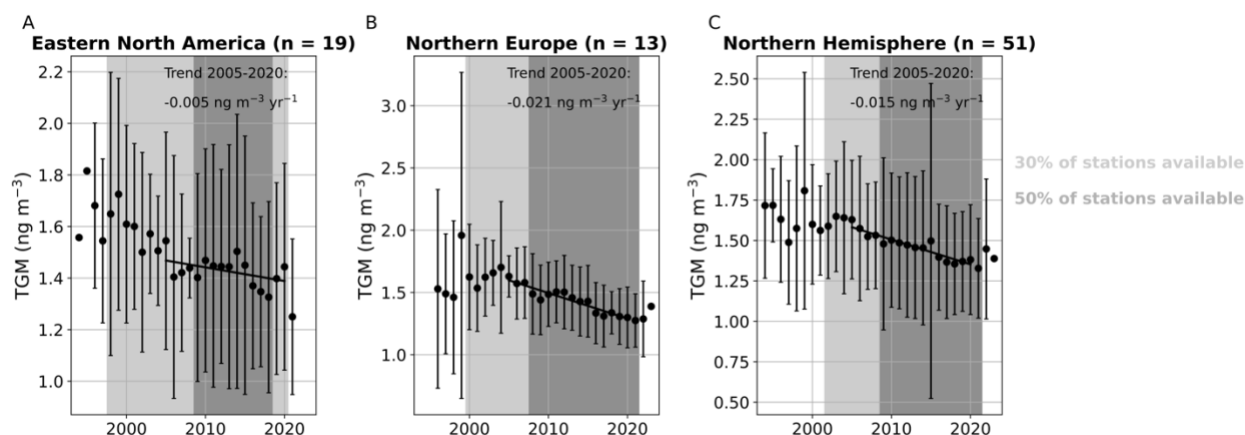108 availability.
109



111 **Figure S3.** "Bucket" method trends calculated by averaging all available station data (not
112 deseasonalized) for each year for Eastern North America (*A*), Northern Europe (*B*), and the overall
113 Northern Hemisphere (*C*). Error bars show the 2σ variation in station averages. Shading shows the years
114 where at least 30% (light gray) and 50% of the stations (dark gray) are available. Linear regression trends
115 are calculated over 2005–2020 and listed on the plot.
116

117 *Section S3.3 Using Generalized Additive Models (GAM) to aggregate multisite data*
118 To test the robustness of our regional trend results to other approaches, we applied the approach of
119 Chang et al. (11) to use Generalized Additive Models (GAM) to aggregate multisite data into an overall
120 trend. In this regression-based approach, we modeled the deseasonalized $Hg^0$ monthly mean values at
121 multiple sites as a function of site ($s$) and time ($t$):
122

123 $$\text{obs}(s,t) = \text{regional trend}(t) + \text{regional seasonality}(t) + \text{site offset}(s) + \text{site-specific trend}(s,t) +$$
124 $$\text{site-specific seasonality}(s,t) + \text{AR(1) error}$$
125 (Eq. S1)
126

127 The GAM approach fits smooth functions of the predictor variables, which include time, month-of-year (for
128 seasonality), and the categorical site ID (for site-specific terms). We used the implementation of GAM in
129 the R package mgcv (12) and calculated fits using the restricted maximum likelihood (REML) method to
130 avoid overfitting.
131

132 The GAM method is not suitable when only a few sites are available within a region (13), so in the main
133 manuscript we focused on linear mixed effect models of regional trends. For the GAM analysis here, we
134 investigated the two regions with more than 10 sites (Eastern North America and Northern Europe). GAM
135 helped to identify nonlinearities in the overall regional trend, for example, a deceleration in the Eastern
136 North America $Hg^0$ decline occurred after ~2009. A previous study has suggested a deceleration in $Hg^0$
137 trends in North America around 2008, although different statistical methods were applied on a smaller set
138 of stations (14). We calculated the 2005–2020 linear trend obtained from the GAM curves for Eastern
139 North America (-0.011 ng m$^{-3}$ yr$^{-1}$) and Northern Europe (-0.019 ng m$^{-3}$ yr$^{-1}$). Since both of these trends
140 are within the error of the results obtained for linear mixed effects modeling (Eastern North America: -
141 0.016 ± 0.011 ng m$^{-3}$ yr$^{-1}$; Northern Europe: -0.018 ± 0.004 ng m$^{-3}$ yr$^{-1}$), we conclude that the derived
142 regional declines are relatively robust to the choice of statistical approach.
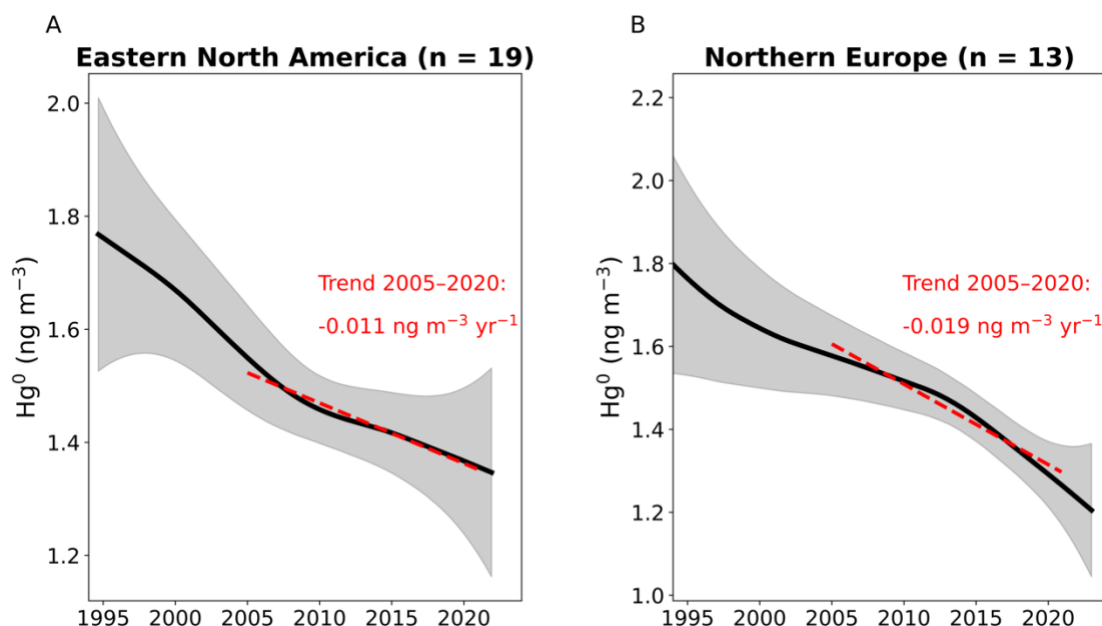
143
144 **Figure S4.** Generalized additive model (GAM) regional trends for multisite deseasonalized total gaseous
145 mercury (Hg⁰) data in Eastern North America (*A*) and Northern Europe (*B*). The GAM mean estimate is
146 shown as a black line, with shaded grey areas showing ± 2 standard errors in the GAM estimate. Linear
147 regression trends (red dashed lines) were calculated over the 2005–2020 period from the regional
148 nonlinear GAM curve.
149
150 *Section S3.4 Restricting the analysis to site data between 2005 and 2020*
151 In the main manuscript (Fig. 2), we use the full set of available data between 1992 and 2022 to calculate
152 linear mixed effects model trends for each region, which are then area-weighted to calculate an average
153 2005–2020 trend for the Northern Hemisphere (NH). We use the full extent of data to maximize the
154 available information in the calculation of long-term Hg⁰ trends. Here, we repeat the analysis but only use
155 data between 2005 and 2020 to calculate the trend, removing all earlier and later data from the analysis.
156 The results are summarized in Fig. S5 and Table S3, which can be compared to Fig. 2 and Table S2.
157 Overall, the regional trends calculated with both datasets are overlapping in their error ranges, with the
158 exception of the Arctic Ocean region (2005–2020: -0.014 ± 0.004 ng m⁻³ yr⁻¹; 1996–2022: -0.007 ± 0.002
159 ng m⁻³ yr⁻¹). The area-weighted NH average trend in the 2005–2020 calculation is -0.015 ± 0.006 ng m⁻³
160 yr⁻¹, slightly more negative but overlapping with the trend calculated in the main paper (-0.011 ± 0.006 ng
161 m⁻³ yr⁻¹). Overall, our conclusions remain the same that the NH Hg⁰ concentrations are declining between
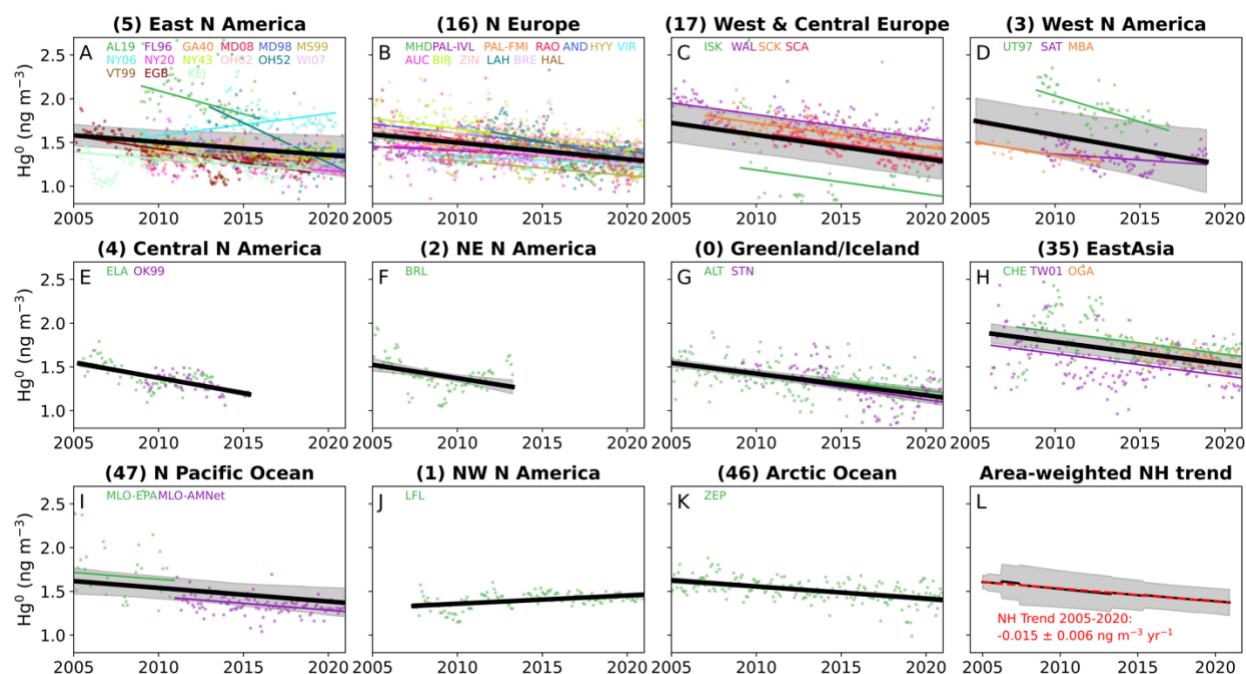162 2005 and 2020 and would be difficult to reconcile with increasing NH anthropogenic emissions.

163
164 **Figure S5.** Similar to Fig. 2 but only for the period of 2005–2020, trends in observed gaseous elemental
165 mercury (Hg$^0$) aggregated by the regions (*A–K*) in Fig. 1 (labelled by region number). Trends are
166 calculated with linear mixed effects modeling, with overall regional trends shown in black and shading
167 shows the 5$^{th}$ to 95$^{th}$ percentile range. Individual site deseasonalized monthly means are shown as
168 colored points and individual regressions as colored lines. The overall Northern Hemisphere (NH) trend
169 (*L*) is calculated by taking the area-weighted average of regional trends, with the shading showing the 2σ
170 averaging error. The red dashed curve in *L* is the linear regression trend for 2005–2020, with trend error
171 representing 2σ error from resampling regional trends within their error bounds.
172
173

174 **Table S3**. Tabulated overall regional trends (± 2σ) calculated through linear mixed effects modelling after
175 restricting site data to 2005–2020 period only. See Table S2 for trends calculated using all data.

| Region name (number) | Number of sites | Area (10^6 km^2) | Trend (ng m^-3 yr^-1) | Time period |
|---|---|---|---|---|
| Eastern North America (5) | 15 | 5.69 | -0.015 ± 0.015 | 2005–2020 |
| Northern Europe (16) | 12 | 5.00 | -0.019 ± 0.006 | 2005–2020 |
| West & Central Europe (17) | 4 | 3.79 | -0.027 ± 0.005 | 2005–2020 |
| Western North America (3) | 3 | 3.14 | -0.034 ± 0.025 | 2005–2018 |
| Central North America (4) | 2 | 2.93 | -0.035 ± 0.007 | 2005–2015 |
| Northeastern North America (2) | 1 | 7.66 | -0.031 ± 0.016 | 2005–2013 |
| Greenland/Iceland (0) | 2 | 4.77 | -0.025 ± 0.008 | 2005–2020 |
| East Asia (35) | 3 | 9.46 | -0.025 ± 0.006 | 2006–2020 |
| North Pacific Ocean (47) | 1 | 51.61 | -0.015 ± 0.011 | 2005–2020 |
| Northwestern North America (1) | 1 | 7.51 | 0.009 ± 0.003 | 2007–2020 |
| Arctic Ocean (1) | 1 | 6.35 | -0.014 ± 0.004 | 2005–2020 |
| **Northern Hemisphere (NH) area-weighted average** | **45** | | **-0.015 ± 0.006** | **2005–2020** |

176
177 **Section S4. Differences between Hg$^0$ and TGM measurements**
178 Atmospheric Hg is measured in three operationally-defined fractions: gaseous elemental mercury (GEM,
179 Hg$^0$), gaseous oxidized mercury (GOM, Hg$^{II}$), and particulate-bound mercury (PBM, Hg$^P$). Total gaseous
180 mercury (TGM) refers to the sum of Hg$^0$ and GOM. Past studies have identified several issues related to
181 the collection of GOM in Tekran instruments, which leads to a low bias of these measurements that can
182 vary over space and time (15–17). For this reason, we do not analyze GOM measurements and focus our
183 analysis on Hg$^0$ . Previous trend analyses have combined measurements of Hg$^0$ and TGM, assuming that
184 Hg$^0$ is the dominant (>98%) fraction of TGM (10, 18, 19). This is supported by analytical studies showing
185 that available TGM measurements from networks do not pick up all GOM, and thus represent a fraction
186 between Hg$^0$ and true TGM (20). Several measurement networks have also suggested that reported TGM
187 measurements largely represent Hg$^0$  concentrations (Environment and Climate Change Canada
188 measurement description; GMOS: Sprovieri et al. (4)). Therefore, in the main manuscript, we assume that
189 available TGM and Hg$^0$ measurements are synonymous and use a combined dataset of these two
190 quantities.
191
192 To test this assumption, we conducted a sensitivity test analyzing trends from only sites where Hg$^0$ data
193 was reported from Tekran or Lumex instruments, removing all TGM data from the analysis. For sites
194 where both Hg$^0$ and TGM data are available (Table S1), we analyzed only the Hg$^0$ data for this sensitivity
195 test. The results of this sensitivity test analyzing only Hg$^0$ are shown in Fig. S6, analogous to Fig. 2 in the
196 main manuscript using the full TGM & Hg$^0$ dataset. For all regions where TGM measurements were
197 removed, the trend estimates resulting from using only Hg$^0$ data overlap with our main manuscript
198 analysis. No clear patterns are observed in the differences between the GEM-only and all data trends,

199  meaning that any differences are probably driven by differences in the data availability and studied time
200  period. The trend estimates are:
201
202  East North America (Fig. S6A) – GEM-only: -0.014 ± 0.016 ng m$^{-3}$ yr$^{-1}$, all data: -0.016 ± 0.011 ng m$^{-3}$ yr$^{-1}$
203  Northern Europe (Fig. S6B) – GEM-only: -0.019 ± 0.007 ng m$^{-3}$ yr$^{-1}$, all data: -0.018 ± 0.004 ng m$^{-3}$ yr$^{-1}$
204  West North America (Fig. S6C) – GEM-only: -0.048 ± 0.026 ng m$^{-3}$ yr$^{-1}$, all data: -0.035 ± 0.025 ng m$^{-3}$ yr$^{-1}$
205  Greenland/Iceland (Fig. S6E) – GEM-only: -0.011 ± 0.004 ng m$^{-3}$ yr$^{-1}$, all data: -0.015 ± 0.003 ng m$^{-3}$ yr$^{-1}$
206  Arctic Ocean (Fig. S6H) – GEM-only: -0.007 ± 0.002 ng m$^{-3}$ yr$^{-1}$, all data: -0.007 ± 0.002 ng m$^{-3}$ yr$^{-1}$
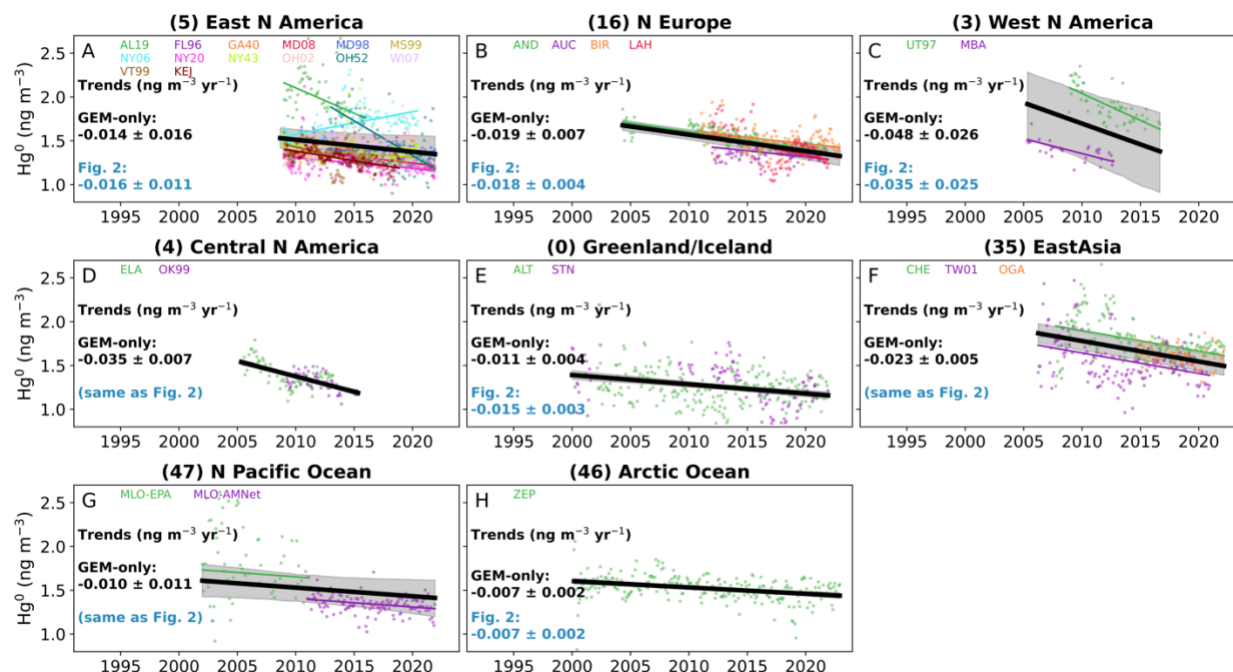207
208



209
210  **Figure S6**. Similar to Fig. 2 but showing only data from Hg$^0$ measurements (removing all TGM
211  measurements from the dataset). Trends in observed gaseous elemental mercury (GEM: Hg$^0$) are
212  aggregated by the regions (A–H) in Fig. 1 (labelled by region number). Trends are calculated with linear
213  mixed effects modeling, with overall regional trends shown in black and shading shows the 5th to 95th
214  percentile range. Listed in black are determined regional trend values from the GEM-only analysis with 2σ
215  errors, while in blue are the trends from the full analysis, including TGM measurements. Three regions
216  only have GEM data and are thus identical to Fig. 2: Central North America, East Asia, and North Pacific
217  Ocean. Due to removal of TGM stations, no data is available from the regions: West & Central Europe,
218  Northeastern North America, and Northwestern North America.
219
220  All other regions either do not have any sites with Hg$^0$ measurements (and thus cannot be evaluated), or
221  have no sites with TGM measurements (and thus are unchanged from the main manuscript analysis).
222  Given the overlapping trend estimates between these two analyses, we conclude that the use of both
223  TGM and Hg$^0$ data does not impact the estimates of the overall regional trends. As well, all trend
224  estimates using only Hg$^0$ data also show negative trends and thus support the conclusions in the main
225  manuscript.
226
227  Our assumption (applied by previous Hg trend studies as well) that TGM and Hg$^0$ measurements can be
228  combined is supported by this sensitivity test where TGM is fully removed from the trend analysis. We

229   therefore chose to keep the analysis using both TGM and Hg$^0$ data in the main manuscript as more
230   locations and time periods are covered.
231
232   **Section S5. Calculating EAME equations from the GBC box model and perturbation analysis**
233   We followed the approach of Selin (21) to calculate parameters from the EAME equation (Eq. 2) using
234   pulse simulations in the Hg Global Biogeochemical Box model (GBC) (22, 23). We introduced an
235   atmospheric Hg pulse of 100 Mg in the year 2010 and monitored the evolution of legacy re-emissions for
236   100 years, until 2110 (Fig. S7). The two-term exponential model fits the behaviour of the box model very
237   well (R$^2$~0.99) on the 100-year time period of the simulation. This fitting reduces the ~40 parameters of
238   the GBC model to 4 understandable parameters, as well as reducing the computation time for legacy re-
239   emissions. We performed a similar experiment by modeling the release of a riverine pulse, and evaluated
240   changes to legacy re-emissions. This equation will differ from the atmospheric pulse, as different
241   timescales are involved (river transport *versus* deposition to oceans) and only a fraction of the riverine
242   pulse will reach the open ocean and not be buried on the coastal shelf.
243
244   To estimate a reasonable range in the legacy re-emission pulse parameters (Eq. 2), we performed 1000
245   parameter perturbation simulations in the GBC model. The 40 relevant parameters that we varied are 35
246   rate coefficients, 3 parameters for the designation of deposition into soil pools, 1 parameter for geogenic
247   emissions, and 1 parameter for the fraction of riverine particulate Hg reaching the open ocean. These
248   parameters were perturbed simultaneously by factors varying between 0.5 and 2, with Latin Hypercube
249   sampling (24) used to ensure that the parameter space is better explored. For each of the 1000
250   experiments, we calculated the legacy re-emission pulse parameters (Eq. 2) and selected the 5$^{th}$–95$^{th}$
251   percentile of each parameter as the range for simulations in the 3-box atmospheric model (Table S4). The
252   1000 experiments were conducted twice, once for atmospheric pulses and once for riverine pulses. The
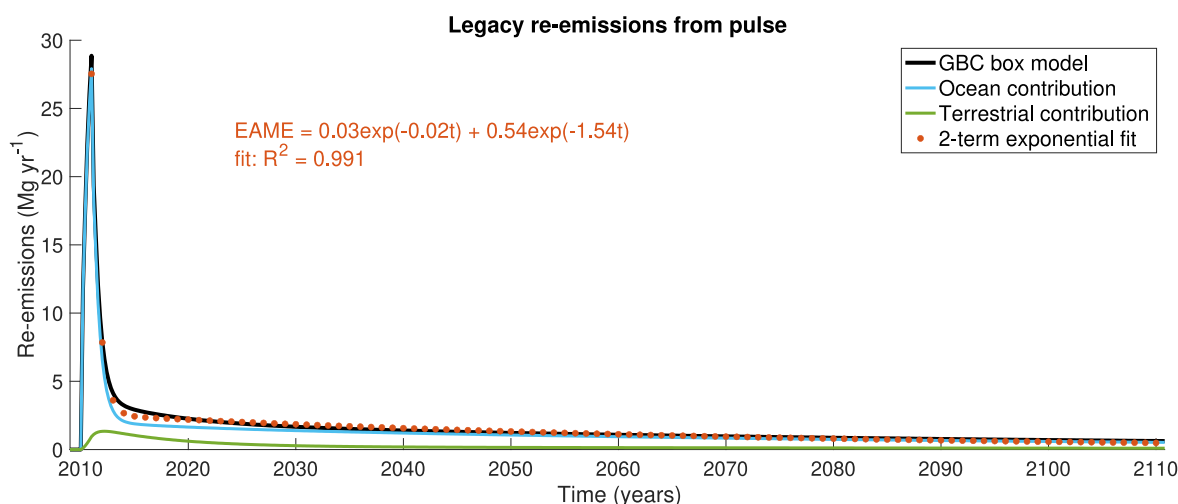253   code for conducting sensitivity experiments in the GBC model is available here:
254   https://github.com/arifein/gbc-boxmodel-sensitivity.



255
256   **Figure S7**. Example of fitting the GBC model pulse experiment to Eq. 2. The contribution of ocean and
257   terrestrial legacy re-emissions to the total are shown as blue and green lines.
258
259
260   **Section S6. 3-box atmospheric model parameter variations**
261   The bounds for the 19 parameters that were varied in the $2 \times 10^5$ simulations, along with their
262   justifications, are listed in Table S4. We sampled the fraction of Hg emitted in the short timescale ($f_{short}$)
263   and the total re-emissions ($E_{total}$) instead of directly sampling coefficients $a_1$ and $a_2$ in Eq. 2. This is less

264   likely to lead to unrealistic combinations of the *a* coefficients and the *b* lifetimes. Integrating Eq. 2
265   between time 0 and infinity yields an equation for $E_{total}$:
266
267
$$E_{total} = a_1 b_1 + a_2 b_2 \qquad\qquad \text{(Eq. S2)}$$
268
269   The fraction of Hg emitted in the short timescale is equal to:
270
271
$$f_{short} = \frac{a_1 b_1}{a_1 b_1 + a_2 b_2} = \frac{a_1 b_1}{E_{total}} \qquad\qquad \text{(Eq. S3)}$$
272
273   We calculated the *a* coefficients from the sampled variables ($b_1$, $b_2$, $f_{short}$, $E_{total}$) using Eq. S4 and Eq. S5:
274
275
$$a_1 = \frac{E_{total}\, f_{short}}{b_1} \qquad\qquad \text{(Eq. S4)}$$
276
$$a_2 = \frac{E_{total}\,(1 - f_{short})}{b_2} \qquad\qquad \text{(Eq. S5)}$$
277
278

279 **Table S4**. Bounds of parameters varied for the 2005–2020 simulations in the 3-box atmospheric model.

| Parameter | Min | Max | Units | Comment/References |
|---|---|---|---|---|
| Atmospheric Hg lifetime | 3 | 8 | months | Horowitz et al. (25); Parrella et al. (26); Zhang et al. (27) |
| Error in 1970 emissions and releases | -20 | +40 | % | Error range suggested for 2000, 2010, 2015 emissions in Streets et al. (28) |
| Error in 1980 emissions and releases | -20 | +40 | % | Error range suggested for 2000, 2010, 2015 emissions in Streets et al. (28) |
| Error in 1990 emissions and releases | -20 | +40 | % | Error range suggested for 2000, 2010, 2015 emissions in Streets et al. (28) |
| Error in 2000 emissions and releases | -20 | +40 | % | Error range suggested for 2000, 2010, 2015 emissions in Streets et al. (28) |
| Error in 2010 emissions and releases | -20 | +40 | % | Error range suggested for 2000, 2010, 2015 emissions in Streets et al. (28) |
| Legacy short lifetime ($b_1$) (atmospheric pulse) | 5.7 | 14.6 | months | Based on perturbation analysis of Amos et al. (22, 23) GBC model (Section S5) |
| Legacy long lifetime ($b_2$) (atmospheric pulse) | 28.6 | 96.9 | years | Based on perturbation analysis of Amos et al. (22, 23) GBC model (Section S5) |
| Legacy fraction emitted in short timescale (atmospheric pulse) | 7 | 31 | % | Based on perturbation analysis of Amos et al. (22, 23) GBC model (Section S5) |
| Total re-emissions from initial pulse (atmospheric pulse) | 79 | 379 | % | Based on perturbation analysis of Amos et al. (22, 23) GBC model (Section S5) |
| Legacy short lifetime ($b_1$) (riverine pulse) | 1.6 | 9.5 | months | Based on perturbation analysis of Amos et al. (22, 23) GBC model (Section S5) |
| Legacy long lifetime ($b_2$) (riverine pulse) | 1 | 116.9 | years | Based on perturbation analysis of Amos et al. (22, 23) GBC model (Section S5) |
| Legacy fraction emitted in short timescale (riverine pulse) | 5 | 55 | % | Based on perturbation analysis of Amos et al. (22, 23) GBC model (Section S5) |
| Total re-emissions from initial pulse (riverine pulse) | 2 | 160 | % | Based on perturbation analysis of Amos et al. (22, 23) GBC model (Section S5) |
| Difference in percent $Hg^0$ emitted from anthropogenic sources between 2020 and 2005 | -20 | 20 | % | The speciation of emissions in longest available inventory (29) varied by 15% (from 60% $Hg^0$ in 1970 to 75% $Hg^0$ in 2010) |
| Anthropogenic emissions trend in Northern Hemisphere (NH) | -70 | 70 | $Mg\ yr^{-2}$ | Covers wide range without 2020 emissions becoming negative |
| Anthropogenic emissions trend in Southern Hemisphere (SH) | -10 | 10 | $Mg\ yr^{-2}$ | Covers wide range without 2020 emissions becoming negative |
| Deviation of releases trend from emissions trend in NH | -80 | 80 | $Mg\ yr^{-2}$ | For example, if NH emissions trend is 30 $Mg\ yr^{-2}$, the NH releases trend ranges between -21 and 139 $Mg\ yr^{-2}$ [*] |
| Deviation of releases trend from emissions trend in NH | -35 | 35 | $Mg\ yr^{-2}$ | For example, if SH emissions trend is -10 $Mg\ yr^{-2}$, the SH releases trend ranges between -45 and 25 $Mg\ yr^{-2}$ [†] |

280 [*] In the NH, decadal release trends in Streets et al. (30) are 1.97 × emissions trends ± 80
281 [†] In the SH, decadal release trends in Streets et al. (30) are 1.03 × emissions trends ± 35
282

283  Fig. S8 visualizes the results of the box model simulations by comparing inputted trends in NH emissions
284  with simulated trends in NH Hg$^0$ over 2005–2020. Fig. S8A displays the relationship between total NH
285  emissions trends (anthropogenic + legacy) and the Hg$^0$ trend. The NH total emissions trends that would
286  be compatible with the observed Hg$^0$ trends (grey range in Fig. S8A) ranges from -15 Mg yr$^{-2}$ to more than
287  -80 Mg yr$^{-2}$. The relationship between the total emissions trends and the Hg$^0$ trend crosses close to the
288  origin, meaning that with a zero total emissions trend the simulated median Hg$^0$ trend is negligible.
289  However, in the case of the anthropogenic emissions trend plot (Fig. S8B), a zero trend in NH
290  anthropogenic emissions will still lead to a positive Hg$^0$ trend due to increasing legacy emissions (31).
291  The NH anthropogenic emissions trend must be below -8 Mg yr$^{-2}$ in order for the NH Hg$^0$ trend to be
292  negative. Another aspect of Fig. S8 is that relationship between NH Hg$^0$ trends and anthropogenic
293  emissions trends is associated with larger uncertainties (Fig. S8B) than that of total emissions (Fig. S8A),
294  as evidenced by the larger red error bars in Fig. S8B. The relationship between total NH emissions trends
295  and the NH Hg$^0$ concentration trend (Fig. S8A) is mainly affected by uncertainties in the atmospheric Hg
296  lifetime, SH emissions, and speciation trends. However, the relationship of anthropogenic NH emissions
297  with Hg$^0$ concentrations is affected by the uncertain response of legacy emissions to anthropogenic inputs
298  and the trends in releases to water and land that would accompany anthropogenic emissions trends for
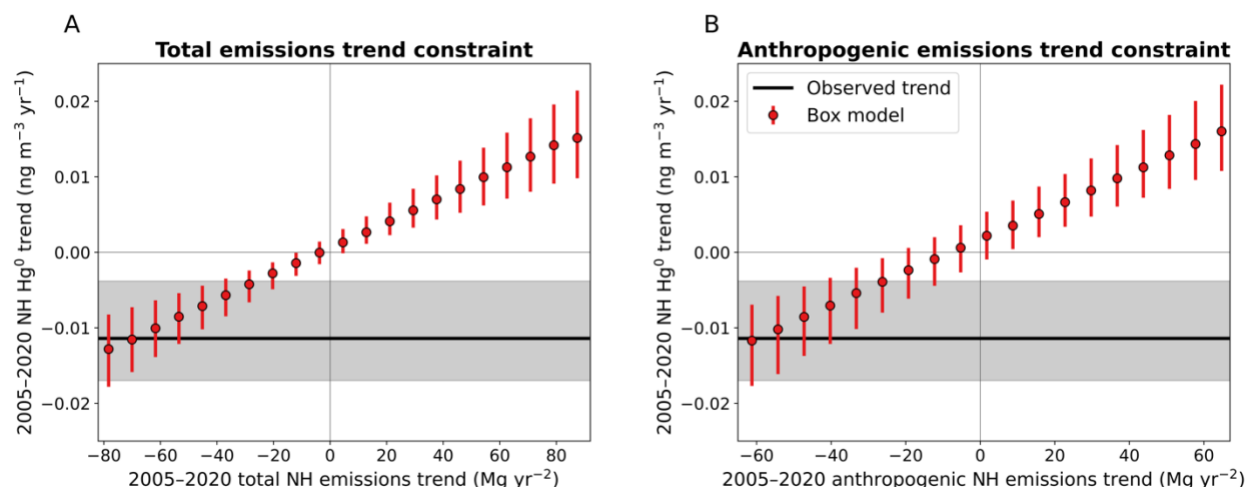299  2005–2020, leading to larger error bars.
300



301
302  **Figure S8**. (*A*) Relationship between NH Hg$^0$ trends and the trends in total NH emissions. The 10$^5$ box
303  model simulations are summarized in the red points (median) and error bars (5$^{th}$ to 95$^{th}$ percentile).
304  Observed NH TGM trends are shown in the horizontal black line, with the associated error shaded. The
305  overlap between grey shading and red error bars represents the parameter space where the model is
306  compatible with observed trends. (*B*) Relationship between NH Hg$^0$ trends and trends in anthropogenic
307  NH emissions. Fig. 3A in the main manuscript represents a 1-D representation of these curves for
308  selected values of the anthropogenic NH emissions trend.
309

310   The relationships between NH Hg re-emissions trends (2005–2020) and anthropogenic emissions and
311   releases parameters in the 3-box model results are plotted in Fig. S9. We have used Fig. S9F in the main
312   paper to relate the trend in NH anthropogenic emissions from the GEOS-Chem scenarios with the
313   expected NH trend in legacy re-emissions. This relationship was used to identify potential trends in legacy
314   emissions resulting from anthropogenic emissions trends, which can then be incorporated in the GEOS-
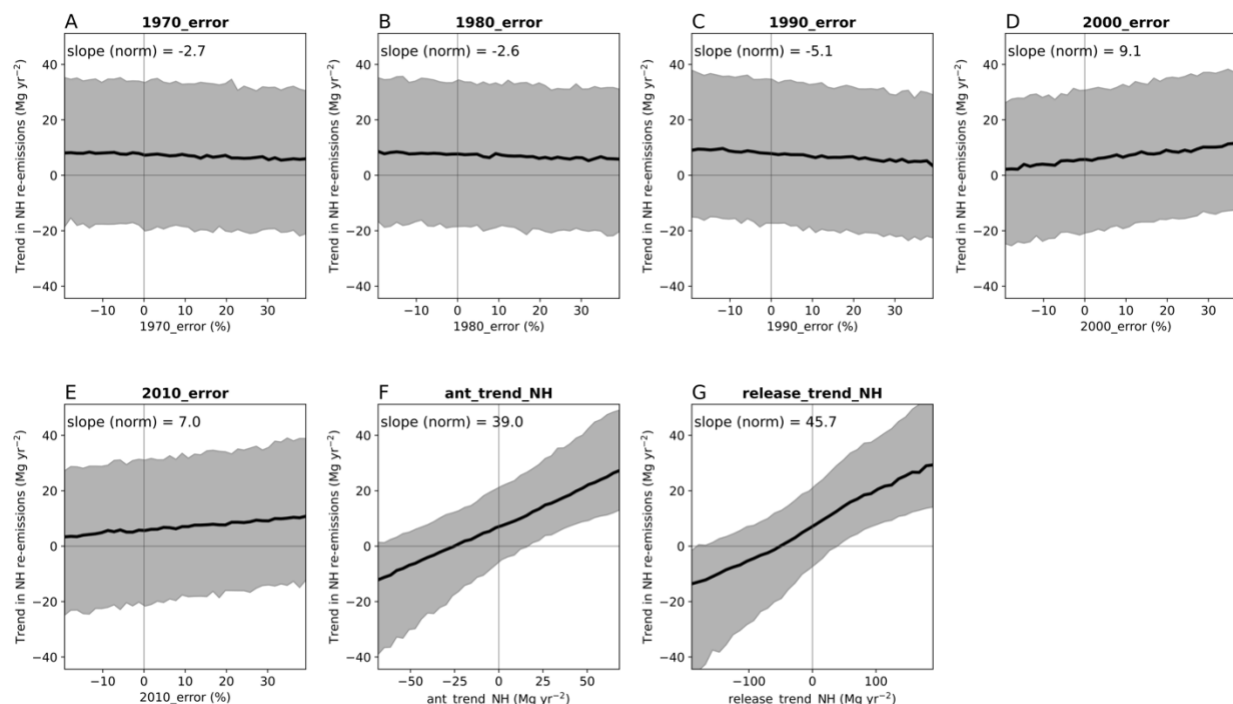315   Chem simulations by scaling ocean Hg$^0$ concentrations.
316



317
318   **Figure S9**. The relationships between Northern Hemisphere (NH) Hg re-emissions trends (2005–2020)
319   and anthropogenic emissions and releases parameters. Plots show the relationship for (*A*) the error in
320   emissions and releases for 1970 in the Streets et al. (30) inventory; (*B*) the error in emissions and
321   releases for 1980; (*C*) the error in emissions and releases for 1990; (*D*) the error in emissions and
322   releases for 2000; (*E*) the error in emissions and releases for 2010; (*F*) the trend in anthropogenic NH
323   emissions for 2005–2020; (*G*) the trend in anthropogenic NH releases for 2005–2020. Black lines show
324   median responses and the shaded area shows the 90% confidence interval (5th to 95th percentile). The
325   slope (normalized to the range of the x-axis parameter) is listed on the plot to illustrate the relative
326   importance of a parameter.
327
328

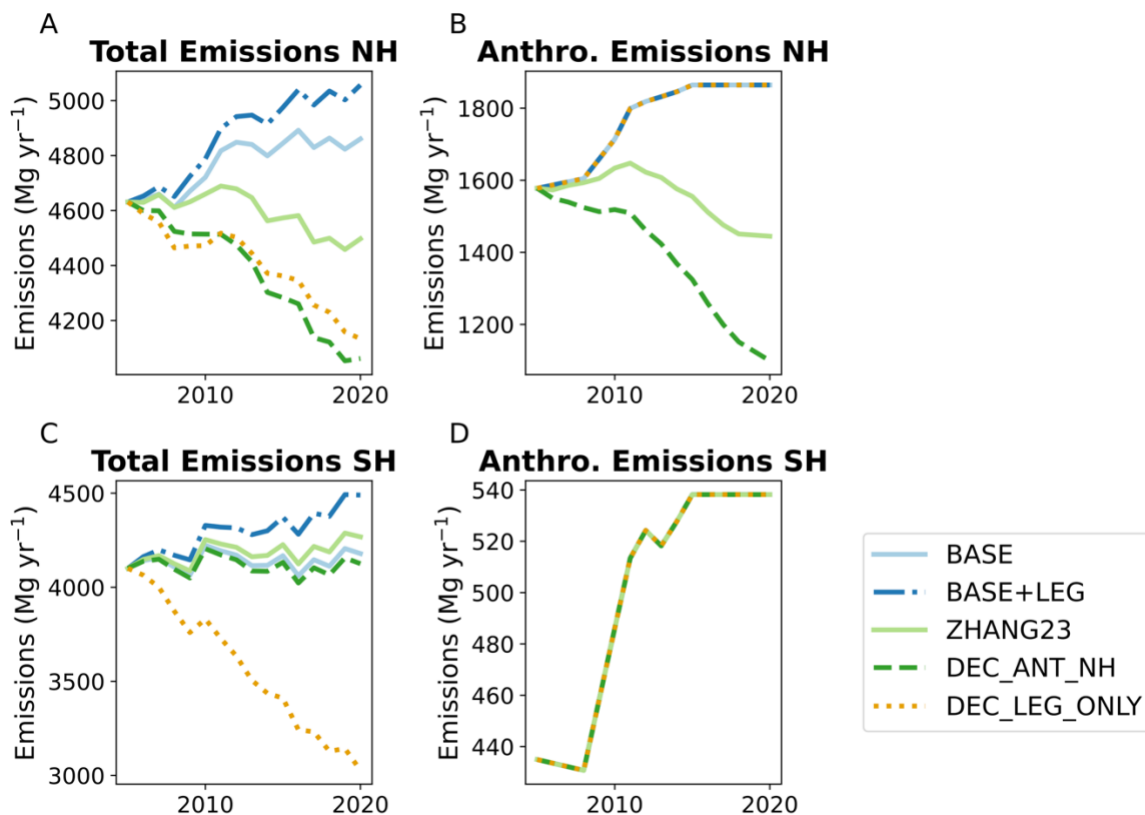329 **Section S7. Description of GEOS-Chem simulations**
330



331
332 **Figure S10.** The emission timeseries in GEOS-Chem simulations for 2005–2020: total emissions in the
333 Northern Hemisphere (*A*), anthropogenic emissions in the Northern Hemisphere (*B*), total emissions in
334 the Southern Hemisphere (*C*), and anthropogenic emissions in the Southern Hemisphere (*D*).
335
336

337   **Section S8. Dry deposition trend in GEOS-Chem simulations**
338   The Leaf Area Index (LAI) data used in GEOS-Chem comes from a reprocessed version of the Moderate
339   Resolution Imaging Spectroradiometer (MODIS) satellite product (32), and includes the observed
340   interannual variations in vegetation. Our GEOS-Chem simulations thus include the impact of (LAI)
341   variations during 2005–2020 on the dry deposition of $Hg^0$. The dry deposition scheme of GEOS-Chem
342   and its response to changes in LAI have been thoroughly evaluated against observations by previous
343   studies (33, 34). Here we evaluate the trends in the NH dry deposition of $Hg^0$ to investigate whether it is a
344   major driver of the $Hg^0$ trends between 2005–2020.
345
346   Figure S11A shows the GEOS-Chem simulated fluxes of dry deposition over the BASE+LEG simulation.
347   The dry deposition flux in the NH increases by 17 $Mg\ yr^{-2}$ over the simulation, yet this is mainly due to the
348   increasing emissions in the BASE+LEG scenario (+31 $Mg\ yr^{-2}$ trend over simulation) increasing the
349   amount of $Hg^0$ in the atmosphere. By dividing the NH $Hg^0$ burden by the dry deposition flux, we can
350   calculate the dry deposition lifetime in the NH over the simulation (Fig. S11B). One observes a slight
351   decline in the lifetime of $Hg^0$ dry deposition in the GEOS-Chem simulations over this time period, with a
352   total decline in the lifetime of 3% between 2005 and 2020. Thus GEOS-Chem shows that the NH dry
353   deposition of $Hg^0$ is indeed becoming faster over this time period, but not to the extent that it would
354   reverse the emission driven changes in $Hg^0$ (Fig. 3C). Therefore, although it is important to further
355   evaluate the impacts of changing vegetation on Hg cycling and its evolution in the future, during the
356   2005–2020 time period the dry deposition lifetime trends have a small impact compared to the estimated
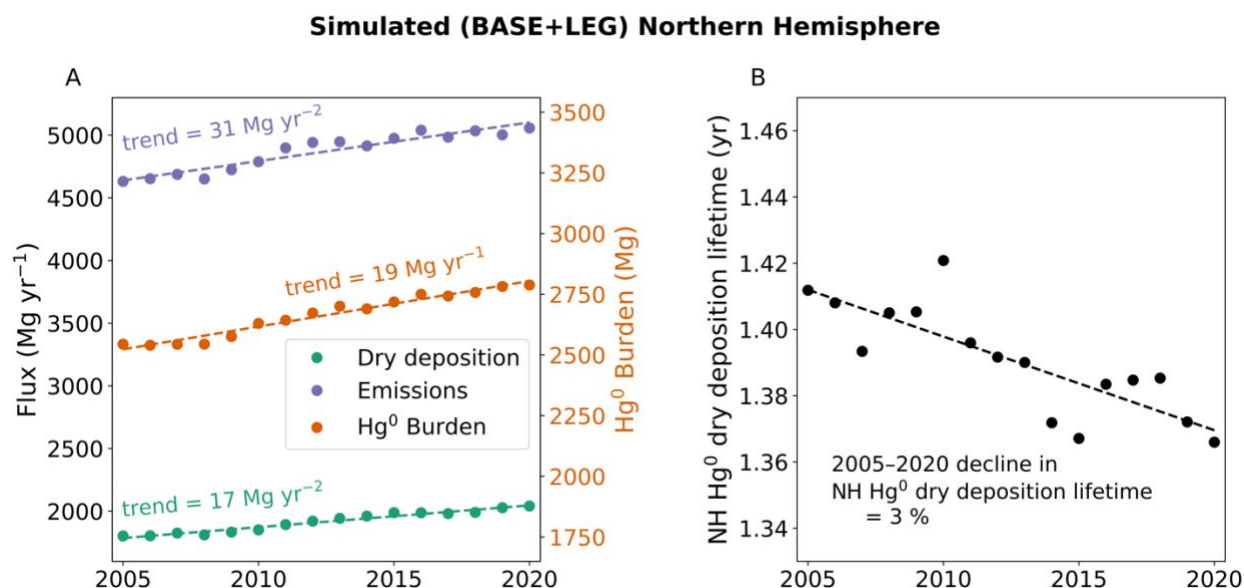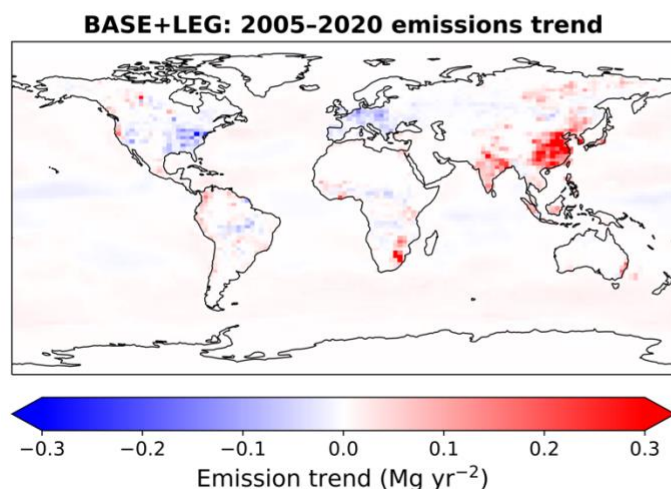357   changes in anthropogenic Hg emissions.
358



359
360   **Figure S11.** Impacts of changing vegetation on the dry deposition of $Hg^0$ in the NH. (*A*) Trends in the NH
361   fluxes of dry deposition and total emissions in the BASE+LEG simulation (left y axis), along with changes
362   in the NH $Hg^0$ burden (right y axis). Linear trend values are listed on the plot. (*B*) Trend in the $Hg^0$ NH dry
363   deposition lifetime over the simulation, with the relative change between 2005 and 2020 listed on the plot.
364

365     **Section S9. Additional quantile regression plots**
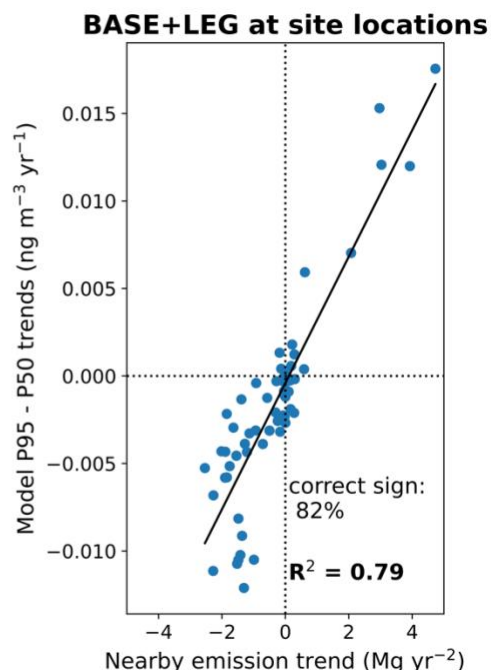366

A



B



367
368     **Figure S12.** (*A*) Map of the linear trend of Hg emissions in the BASE+LEG simulation between 2005 and
369     2020. (*B*) Comparing the relationship between the BASE+LEG simulated nearby emission trend and the
370     difference between the 95th percentile (P95) and median (P50) quantile regression Hg$^0$ trends at grid
371     boxes corresponding to site locations (see Fig. 4C for the full P95 – P50 trends map). The nearby
372     emission trend is calculated by summing emissions trends within two grid boxes (~500 km) of the site
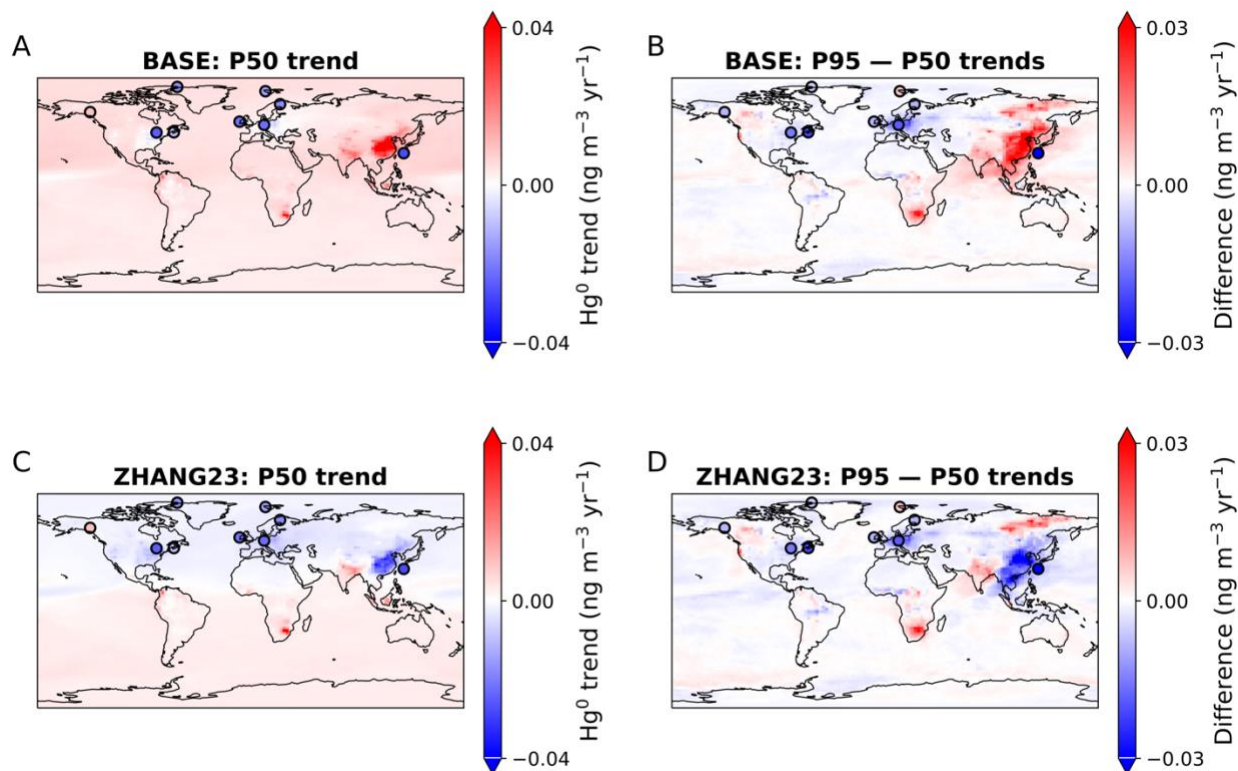373     location grid box.
374

375
376 **Figure S13.** Trend in median (P50) daily deseasonalized simulated values in BASE (*A*) and ZHANG23
377 (*C*) for each model grid cell. Observed results are plotted in filled circles for 9 stations with more than 13
378 years of high frequency data. Differences between 95th percentile (P95) trend and median (P50) trend
379 shown for BASE (*B*) and ZHANG23 (*D*) simulations and observations. The other simulations
380 (BASE+LEG, DEC_ANT_NH, and DEC_LEG_ONLY) are shown in Fig. 4.

381 **Section S10. Additional comparisons between observations and model simulations**
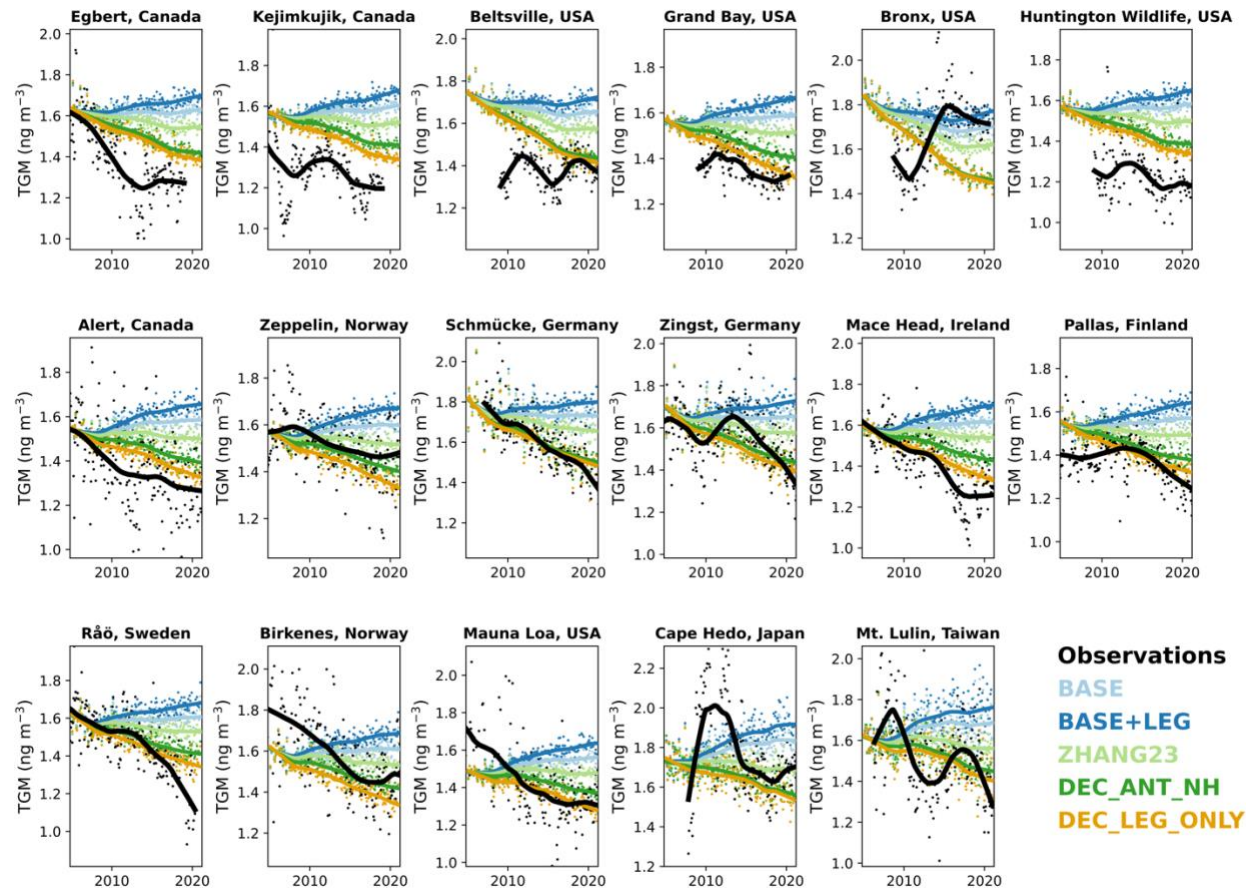382



383
384 **Figure S14.** Timeseries plots comparing model simulations (colors) and observations (black) at stations
385 with more than 12 years of data during 2005–2020. Markers show deseasonalized monthly means and
386 lines show the smoothed tendency of the time series calculated using LOWESS (locally weighted
387 scatterplot smoothing) regression.
388

389 **Section S11. EDGAR v8.1_toxHg emissions inventory**
390 A new anthropogenic emissions inventory has recently been released for 1970–2022, the EDGAR
391 v8.1_toxHg inventory (35). Compared to the previous iteration of this inventory (EDGAR v4.tox2) (29),
392 the v8.1 inventory includes updated spatial proxies and emissions factors and is extended to 2020. The
393 released speciation maps ($Hg^0$, $Hg^{2+}$, $Hg^P$) from the inventory were still in draft form at the time of this
394 manuscript, so we did not run GEOS-Chem simulations with v8.1_toxHg, though this will be upcoming in
395 the MCHgMAP project (36). The total Hg emissions maps have been released in definitive form at this
396 time, so we have analyzed the trends in the total emissions (Fig. S15). The NH trend between 2005 and
397 2020 is 35 Mg $yr^{-2}$, very similar to the Streets et al. (28) 2005–2015 trend (34 Mg $yr^{-2}$). Therefore, our
398 modelling results using the Streets et al. (28) emissions trends are likely applicable to the new EDGAR
399 v8.1_toxHg inventory as well. Increasing global and NH emissions are a common feature in both Streets
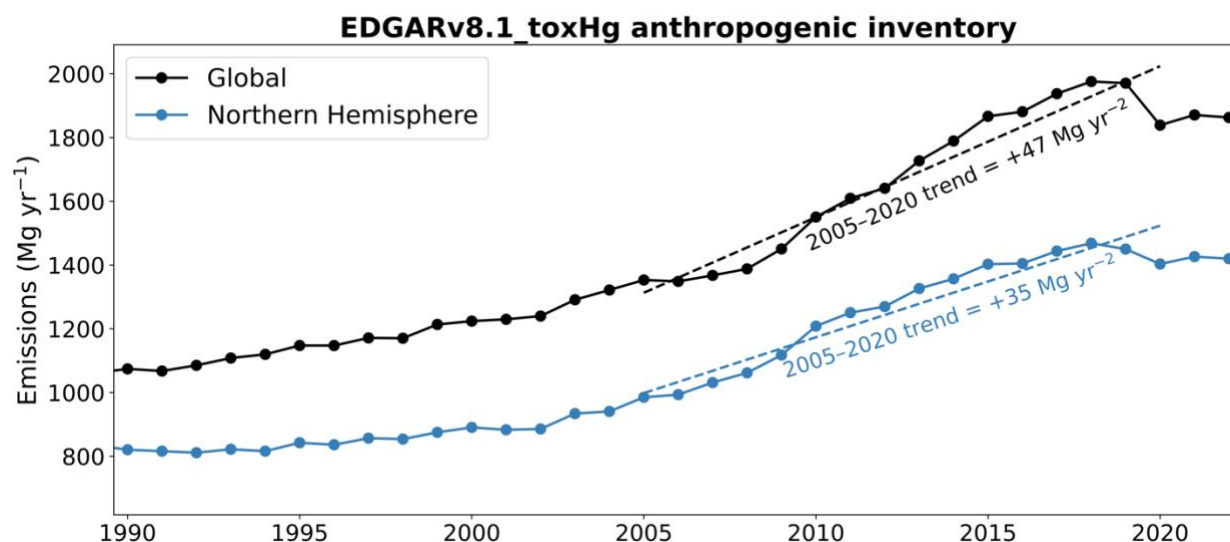400 et al. (28) and EDGAR v8.1_toxHg inventories, in contrast to the observed decline in $Hg^0$ concentrations.
401

402


403 **Figure S15.** Anthropogenic emissions trend from the EDGARv8.1_tox anthropogenic inventory, with
404 linear trends calculated and plotted for the 2005–2020 period.
405

406 **Supplementary References**
407 1.    M. Iturbide, *et al.*, An update of IPCC climate reference regions for subcontinental analysis of
408        climate model data: definition and aggregated datasets. *Earth Syst. Sci. Data* **12**, 2959–2970
409        (2020).
410 2.    D. A. Gay, *et al.*, The Atmospheric Mercury Network: measurement and initial examination of an
411        ongoing atmospheric mercury record across North America. *Atmos. Chem. Phys.* **13**, 11339–11349
412        (2013).
413 3.    F. Carbone, *et al.*, Sea surface temperature variation linked to elemental mercury concentrations
414        measured on Mauna Loa. *Geophys. Res. Lett.* **43**, 7751–7757 (2016).
415 4.    F. Sprovieri, *et al.*, Atmospheric mercury concentrations observed at ground-based monitoring sites
416        globally distributed in the framework of the GMOS network. *Atmos. Chem. Phys.* **16**, 11915–11935
417        (2016).
418 5.    A. Cole, *et al.*, A Survey of Mercury in Air and Precipitation across Canada: Patterns and Trends.
419        *Atmosphere* **5**, 635–668 (2014).
420 6.    V. L. St. Louis, *et al.*, Atmospheric Concentrations and Wet/Dry Loadings of Mercury at the Remote
421        Experimental Lakes Area, Northwestern Ontario, Canada. *Environ. Sci. Technol.* **53**, 8017–8026
422        (2019).

423   7.    K. Tørseth, *et al.*, Introduction to the European Monitoring and Evaluation Programme (EMEP) and
424        observed atmospheric composition change during 1972–2009. *Atmos. Chem. Phys.* **12**, 5447–5481
425        (2012).

426   8.    L. S. P. Nguyen, G.-R. Sheu, D.-W. Lin, N.-H. Lin, Temporal changes in atmospheric mercury
427        concentrations at a background mountain site downwind of the East Asia continent in 2006–2016.
428        *Science of The Total Environment* **686**, 1049–1056 (2019).

429   9.    K. Marumoto, *et al.*, Long-Term Observation of Atmospheric Speciated Mercury during 2007–2018
430        at Cape Hedo, Okinawa, Japan. *Atmosphere* **10**, 362 (2019).

431   10.   Y. Zhang, *et al.*, Observed decrease in atmospheric mercury explained by global decline in
432        anthropogenic emissions. *Proc. Natl. Acad. Sci. U.S.A.* **113**, 526–531 (2016).

433   11.   K.-L. Chang, *et al.*, Trend detection of atmospheric time series. *Elementa: Science of the
434        Anthropocene* **9**, 00035 (2021).

435   12.   S. N. Wood, Fast stable restricted maximum likelihood and marginal likelihood estimation of
436        semiparametric generalized linear models. *Journal of the Royal Statistical Society (B)* **73**, 3–36
437        (2011).

438   13.   K.-L. Chang, M. G. Schultz, G. Koren, Selke, Niklas, Guidance note on best statistical practices for
439        TOAR analyses. Available at: https://doi.org/10.48550/arXiv.2304.14236. (2023).

440   14.   P. S. Weiss-Penzias, *et al.*, Trends in mercury wet deposition and mercury air concentrations across
441        the U.S. and Canada. *Science of The Total Environment* **568**, 546–556 (2016).

442   15.   M. S. Gustin, *et al.*, Measurement of Atmospheric Mercury: Current Limitations and Suggestions for
443        Paths Forward. *Environ. Sci. Technol.* **58**, 12853–12864 (2024).

444   16.   M. S. Gustin, *et al.*, Do We Understand What the Mercury Speciation Instruments Are Actually
445        Measuring? Results of RAMIX. *Environ. Sci. Technol.* **47**, 7295–7306 (2013).

446   17.   A. Steffen, *et al.*, A synthesis of atmospheric mercury depletion event chemistry in the atmosphere
447        and snow. *Atmospheric Chemistry and Physics* **8**, 1445–1482 (2008).

448   18.   K. MacSween, *et al.*, Updated trends for atmospheric mercury in the Arctic: 1995–2018. *Science of
449        The Total Environment* **837**, 155802 (2022).

450   19.   D. Custódio, *et al.*, Odds and ends of atmospheric mercury in Europe and over the North Atlantic
451        Ocean: temporal trends of 25 years of measurements. *Atmos. Chem. Phys.* **22**, 3827–3840 (2022).

452   20.   J. Gačnik, S. Lyman, S. M. Dunham-Cheatham, M. S. Gustin, Limitations and insights regarding
453        atmospheric mercury sampling using gold. *Analytica Chimica Acta* **1319**, 342956 (2024).

454   21.   N. E. Selin, A proposed global metric to aid mercury pollution policy. *Science* **360**, 607–609 (2018).

455   22.   H. M. Amos, D. J. Jacob, D. G. Streets, E. M. Sunderland, Legacy impacts of all-time anthropogenic
456        emissions on the global mercury cycle. *Global Biogeochem. Cycles* **27**, 410–421 (2013).

457   23.   H. M. Amos, *et al.*, Global Biogeochemical Implications of Mercury Discharges from Rivers and
458        Sediment Burial. *Environ. Sci. Technol.* **48**, 9514–9522 (2014).

459   24.   M. D. McKay, R. J. Beckman, W. J. Conover, Comparison of Three Methods for Selecting Values of
460        Input Variables in the Analysis of Output from a Computer Code. *Technometrics* **21**, 239–245
461        (1979).

462   25.   H. M. Horowitz, *et al.*, A new mechanism for atmospheric mercury redox chemistry: implications for
463        the global mercury budget. *Atmos. Chem. Phys.* **17**, 6353–6371 (2017).

464   26.   J. P. Parrella, *et al.*, Tropospheric bromine chemistry: implications for present and pre-industrial
465        ozone and mercury. *Atmos. Chem. Phys.* **12**, 6723–6740 (2012).

466   27.   Y. Zhang, *et al.*, An updated global mercury budget from a coupled atmosphere-land-ocean model:
467        40% more re-emissions buffer the effect of primary emission reductions. *One Earth* **6**, 316–325
468        (2023).

469   28.   D. G. Streets, *et al.*, Global and regional trends in mercury emissions and concentrations, 2010–
470        2015. *Atmospheric Environment* **201**, 417–427 (2019).

471   29.   M. Muntean, *et al.*, Evaluating EDGARv4.tox2 speciated mercury emissions ex-post scenarios and
472        their impacts on modelled global and regional wet deposition patterns. *Atmospheric Environment*
473        **184**, 56–68 (2018).

474   30.   D. G. Streets, *et al.*, Five hundred years of anthropogenic mercury: spatial and temporal release
475        profiles. *Environ. Res. Lett.* **14**, 084004 (2019).

476   31.   H. Angot, *et al.*, Global and Local Impacts of Delayed Mercury Mitigation Efforts. *Environ. Sci.
477        Technol.* **52**, 12968–12977 (2018).

478    32.   H. Yuan, Y. Dai, Z. Xiao, D. Ji, W. Shangguan, Reprocessing the MODIS Leaf Area Index products
479          for land surface and climate modelling. *Remote Sens. Environ.* **115**, 1171–1187 (2011).
480    33.   A. Feinberg, T. Dlamini, M. Jiskra, V. Shah, N. E. Selin, Evaluating atmospheric mercury (Hg)
481          uptake by vegetation in a chemistry-transport model. *Environ. Sci.: Processes Impacts* **24**, 1303–
482          1318 (2022).
483    34.   A. Feinberg, M. Jiskra, P. Borrelli, J. Biswakarma, N. E. Selin, Deforestation as an Anthropogenic
484          Driver of Mercury Pollution. *Environ. Sci. Technol.* **58**, 3246–3257 (2024).
485    35.   M. Muntean, *et al.*, EDGAR v8.1 Global Mercury Emissions. European Commission, Joint Research
486          Centre (JRC) [Dataset] PID: http://data.europa.eu/89h/83b507d7-5218-4dc5-95f9-0ec36f073204.
487          Deposited 2024.
488    36.   A. Dastoor, *et al.*, The Multi-Compartment Hg Modeling and Analysis Project (MCHgMAP): Mercury
489          modeling to support international environmental policy. *Geoscientific Model Development*
490          *Discussions* **2024**, 1–171 (2024).

491